

# NEURALPLANE: STRUCTURED 3D RECONSTRUCTION IN PLANAR PRIMITIVES WITH NEURAL FIELDS

**Anonymous authors**

Paper under double-blind review

## ABSTRACT

3D maps assembled from planar primitives are compact and expressive in representing man-made environments, making them suitable for a spectrum of applications. In this paper, we present **NeuralPlane**, a novel approach that explores **neural** fields for multi-view 3D **plane** reconstruction. Our method is centered upon the core idea of distilling geometric and semantic cues from inconsistent 2D plane observations into a unified 3D neural representation, which unlocks the full leverage of plane attributes. This idea is accomplished by NeuralPlane through several key designs, including: 1) a monocular module that generates geometrically smooth and semantically meaningful segments as 2D plane observations, 2) a plane-guided training procedure that implicitly learns accurate plane locations from multi-view plane observations, and 3) a self-supervised feature field termed Neural Coplanarity Field that enables the modeling of scene semantics alongside the geometry. Without relying on plane annotations, our method achieves high-fidelity reconstruction comprising planar primitives that are not only crisp but also well-aligned with the semantic content. Comprehensive experiments on ScanNetv2 and ScanNet++ demonstrate the superiority of our results in both geometry and semantics. Our project page: <https://neuralplane.github.io/>.

## 1 INTRODUCTION

While inferring dense geometry such as volumetric grids and meshes from 2D images has been extensively studied (Schönberger et al., 2016; Murez et al., 2020; Wu et al., 2023b), there is also a growing realization that reconstructs *sparse 3D maps composed of self-contained primitives* (Xue et al., 2024; Li et al., 2024; Kluger et al., 2024; Mazur et al., 2024). In this paper, we focus on reconstructing structured indoor scenes as configurations of *planar primitives*. Among the most common geometric primitives, such as line segments and edges, planar primitives are particularly instrumental in describing man-made environments. Furthermore, they are compact and expressive parametric entities that provide not only strong geometric cues, but also rich semantic information. From this lens, 3D maps built by planar primitives are notably lean and convenient for practical use, and have been successfully deployed in various applications in areas such as robotics (Zhou et al., 2021; Liu et al., 2023) and augmented reality (ARKit, 2024; ARCore, 2024).

The reconstruction of 3D planes is conventionally approached by fitting planar primitives to an unordered point cloud or a mesh generated from depth sensors or multi-view stereo (Yu & Lafarge, 2022). The input geometries of these methods are typically noisy and incomplete, and provide only limited semantic information for robust plane detection. A recent work by Watson et al. (2024) incorporates optimized 3D semantic embeddings into the plane fitting module, *i.e.*, RANSAC (Fischler & Bolles, 1981), which helps to discern adjacent planes. However, it still heavily relies on the quality of input geometry, and requires to train from additional plane annotations. These prior efforts basically decouple 3D plane reconstruction as two independent problems of non-plane-biased geometry recovery and plane estimation, which bottlenecks the full utilization of plane attributes. Departing from such geometry+RANSAC paradigm, Xie et al. (2022) developed the first learning-based model that incrementally reconstructs planes from posed video fragments. However, though supervised by 3D plane annotations, the method struggles with its adaptability to intricate structures.

Motivated by previous limitations, as well as the success of neural fields in sparse geometry encoding (Ye et al., 2023; Xue et al., 2024; Li et al., 2024) and 3D segmentation (Ying et al., 2024; Kim

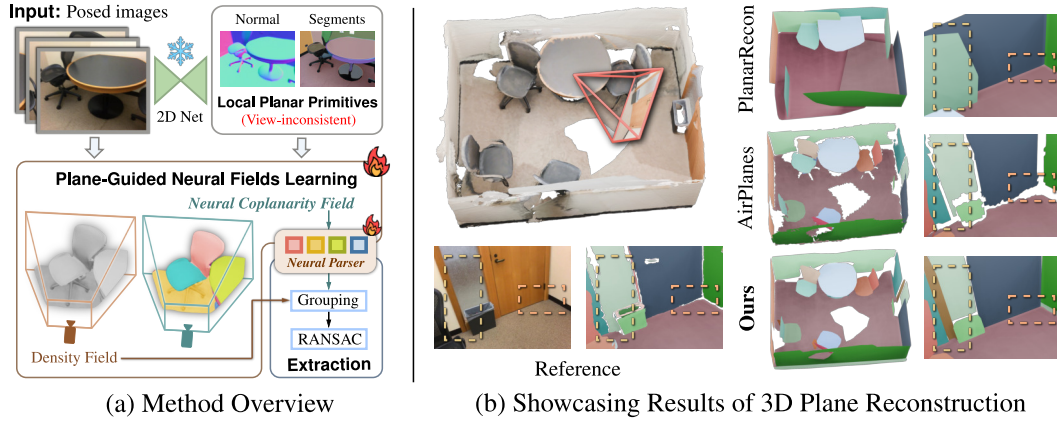


Figure 1: **Structured 3D reconstruction in planar primitives with neural fields.**

et al., 2024), we introduce a new approach named **NeuralPlane**. The proposed method maintains a consistent neural representation for environmental plane structures from multi-view inconsistent plane observations, which further enables the extraction of high-quality 3D planar primitives.

Fig. 1 (a) provides an overview of our pipeline, which unfolds into three phases: 1) Firstly, we combine two robust vision models into a training-free module capable of excavating well-defined plane segments from a single image. Plane parameters of these segments are initialized simultaneously, yielding a set of locally estimated 3D entities referred to as Local Planar Primitives. 2) Secondly, we design a plane-guided training procedure where the high degree of *intra-primitive* geometric regularity is explored to optimize the density field. Although this effectively mitigates the issue of poor surface reconstruction when encoding the scene geometry by volume density, we recognize that the density field alone is insufficient for extracting *semantically well-aligned* planar primitives. Thereby, we also propose Neural Coplanarity Field, a self-supervised feature field that involves high-level semantics. This neural field utilizes local planar primitives for *inter-primitive* reasoning within a contrastive learning framework, and can accurately capture the *coplanar relationships* between different regions. 3) Finally, on top of the learned neural representation, we conduct a two-stage plane extraction process. Before geometrically fitting planar primitives, the neural representation is grouped into isolated regions based on the learned coplanarity features, wherein a novel module called Neural Parser is introduced to facilitate the discrimination of plane instances.

Fig. 1 (b) showcases the superiority of our NeuralPlane over existing state-of-the-arts (Xie et al., 2022; Watson et al., 2024), where our method faithfully rebuilds scene layouts as sets of crisp planar primitives while preserving fine-grained semantics. In summary, our key contributions are:

- We present NeuralPlane, a novel approach for multi-view 3D plane reconstruction that eschews plane annotations. It enjoys the synergy between geometry and semantics in the context of neural fields and achieves leading performance in extensive experimental studies.
- To capture accurate plane locations, a self-prompting mechanism that integrates two robust vision models is first proposed to excavate 2D plane regions, wherein strong plane regularity is then applied to guide the optimization of the implicitly encoded geometry.
- We enhance plane discrimination by incorporating semantics: Neural Coplanarity Field acts as the core driver of involving the semantic separation via contrastive learning, while Neural Parser is introduced to jointly model the learned coplanar relationships.

## 2 RELATED WORK

### 2.1 MULTI-VIEW PLANE RECONSTRUCTION

The basis of 3D plane reconstruction from multi-view images lies in the detection of planar regions from either raw RGB inputs or inferred dense geometries. Despite impressive progress in single view

plane detection (Yang & Zhou, 2018; Liu et al., 2019; Yu et al., 2019), a unified multi-view plane reconstruction remains challenging due to severe cross-view inconsistencies. Several attempts have been made to locally recover 3D planes from a limited number of images by predicting plane correspondences (Jin et al., 2021; Agarwala et al., 2022; Tan et al., 2023) or stereo matching (Liu et al., 2022). However, scaling to multi-view scenarios for global reconstructions is still problematic. More related to us, PlanarRecon (Xie et al., 2022) is the first learning-based model that reconstructs 3D plane maps by incrementally detecting, tracking, and fusing 3D planes from posed video fragments. Chen et al. (2023) draw upon neural fields to detect planar primitives from RGB-D sequences. AirPlanes (Watson et al., 2024) benefits from the conventional two-stage pipeline of fitting planes to non-plane-biased geometry inferred by an efficient 3D surface reconstruction method (Sayed et al., 2022), while lifting the learned 2D plane priors into 3D for robust plane distinction.

## 2.2 HIGHER-LEVEL MAPPING VIA NEURAL RENDERING

Neural rendering has emerged as a powerful technique that allows distilling various 2D observations from multiple views into 3D neural fields. It has greatly reshaped a wide range of 3D scene reconstruction and understanding tasks. Recent works (Ye et al., 2023; Xue et al., 2024; Li et al., 2024) find the neural field favorable for implicitly encoding *sparse parametric primitives* such as line segments and edges. Object-compositional neural representations have also been extensively explored for *object-centric mapping* (Yang et al., 2021; Yu et al., 2022a; Wang et al., 2023; Park et al., 2024). Besides, there are advances in constructing *semantic maps* with neural fields by distilling high-dimensional features (Kobayashi et al., 2022; Kerr et al., 2023) or optimizing a contrastive loss (Fan et al., 2023; Bhalgat et al., 2023; Kim et al., 2024). Our study falls within the exploration of neural fields for parametric primitives. However, rather than focusing solely on geometry, we also integrate semantics to construct the neural representation from a broader perspective.

## 3 METHOD: NEURALPLANE

Given a set of posed images, our goal is to recover the underlying scene structure using a collection of 3D planar primitives. To this end, we first process the input images to acquire monocular plane priors known as local planar primitives (Sec. 3.1). Then, we introduce our neural scene representation, which is optimized under the plane guidance (Sec. 3.2). Once optimized, the neural representation is made explicit by our plane extraction algorithm (Sec. 3.3).

### 3.1 GENERATING LOCAL PLANAR PRIMITIVES

Essentially, a local planar primitive  $P = (\mathcal{M} \subseteq I, \pi)$  is defined as a plane segment  $\mathcal{M}$  of a single image  $I$ , associated with plane parameters  $\pi = [\mathbf{n}, o]$  that have been transformed into world space. Here,  $\mathbf{n} \in \mathbb{R}^3$  and  $o \in \mathbb{R}^+$  are respectively the unit normal vector and the offset of the plane from the origin. Although remarkably advanced single-view plane recovery models (Tan et al., 2021; Shi et al., 2023) can be employed to estimate such local planar primitives, we will show that purely local yet robust image priors are sufficient to achieve satisfactory performance, which eliminates the need to deliberately train a model on plane annotations.

**Plane Segments from Monocular Priors.** We define the plane segment  $\mathcal{M}$  of a local planar primitive  $P$  as an image region that (1) has consistent normal directions and (2) is geometrically continuous. To excavate such plane segments from an input image, we repurpose a pre-trained monocular normal predictor (Bae et al., 2021) and the powerful Segment Anything Model (SAM) (Kirillov et al., 2023). Specifically, we start by applying K-means clustering (Lloyd, 1982) to the predicted normal map, obtaining low-frequency regions with each having similar normal directions. Subsequently, SAM’s automatic mask generator is employed to further segment these smooth regions by selecting the smallest mask for each prompt. This over-segmentation using SAM not only allows us to enforce geometric continuity approximately but also produces semantically meaningful segments. Finally, masks exceeding a specified size threshold are chosen as the desired plane segments.

**Initializing Local Plane Geometry.** For each local planar primitive  $P$ , we initialize its plane normal  $\mathbf{n}$  by averaging the predicted normals within the plane segment  $\mathcal{M}$ . Since poses of input images are often estimated by Structure-from-Motion (SfM) systems that concurrently output sparse 3D keypoints, we propose to initialize the plane offset using this readily accessible by-product. Specifi-

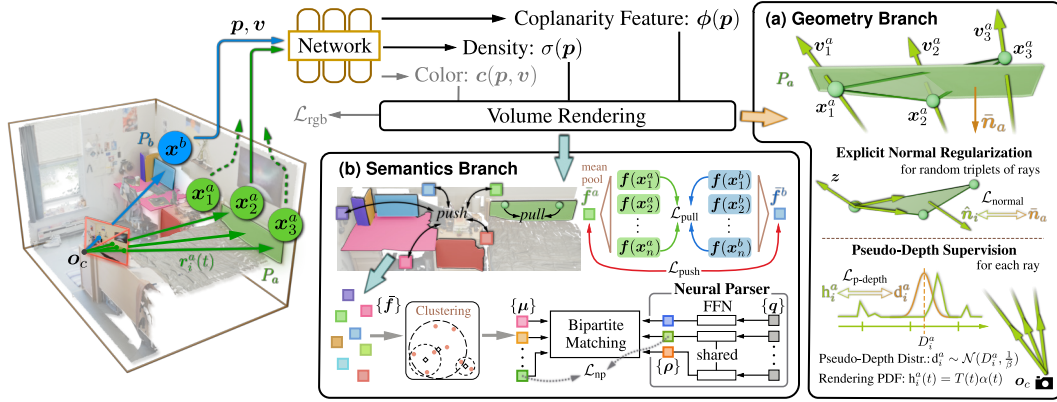


Figure 2: **Plane-guided neural fields learning.** The overall training scheme consists of two branches: (a) the geometry branch (Sec. 3.2.1) translates plane constraints into two intra-primitive regularization terms, i.e.,  $\mathcal{L}_{\text{normal}}$  and  $\mathcal{L}_{\text{p-depth}}$ ; (b) the semantics branch (Sec. 3.2.2) performs inter-primitive reasoning via contrastive learning, and introduces a query-based learning module (Neural Parser) to jointly model the captured coplanar relationships.

cally, the plane offset is initialized by minimizing the total distance from 3D keypoints  $\{p_1, \dots, p_m\}$  detected in  $\mathcal{M}$  to the plane:

$$\bar{o} = \arg \min_{v \in \mathbb{R}^+} \sum_i^m \frac{w_i}{\sum w_i} \|\bar{n} \cdot p_i + v\|_2^2, \quad (1)$$

where  $\bar{n}$  is the initialized plane normal, and the weight  $w_i = 1/\bar{e}_i$ , indicating the reliability of  $p_i$ , is approximated using the average reprojection error  $\bar{e}_i$  across views where  $p_i$  is visible. Though error-prone, the process is sufficient to provide effective geometry guidance for our neural representation, which will be detailed below.

### 3.2 LEARNING NEURAL REPRESENTATION UNDER PLANE GUIDANCE

Note that local planar primitives are generated with minimal dependence on viewpoint, thus resulting in severe inconsistency across views. We acknowledge that it is non-trivial to explicitly establish correspondences and merge them into a compact 3D plane reconstruction. As a consequence, we propose to fuse them implicitly using neural fields. The overall training scheme of our NeuralPlane is illustrated in Fig. 2, which consists of two major branches: 1) the geometry branch (Sec. 3.2.1) focuses on learning accurate plane locations, while 2) the semantics branch (Sec. 3.2.2) captures coplanar relationships between different regions from conflicting 2D plane segments.

#### 3.2.1 GEOMETRY BRANCH

NeuralPlane implicitly encodes scene geometry as volume density. In this section, we translate strong plane constraints provided by generated local planar primitives into two regularization terms to alleviate the well-known *shape-radiance* ambiguity (Zhang et al., 2020).

**Preliminaries.** Standard NeRF (Mildenhall et al., 2020) represents a scene as a continuous volume density function  $\sigma : \mathbb{R}^3 \mapsto [0, 1]$  and a continuous view-dependent color function  $c : (\mathbb{R}^3, \mathbb{S}^2) \mapsto [0, 1]^3$ . According to the volume rendering formula, given a ray  $r$  emanating from camera center  $o_c$  with direction  $v$ , its expected termination point  $x$  is computed by integrating  $N$  sampled points  $\{p_i = o_c + t_i v | i = 1, \dots, N, t_i < t_{i+1}\}$  along the ray:

$$x = \sum_{i=1}^N h(t_i) p_i, \quad h(t_i) = T(t_i) \alpha(t_i) = \left( \prod_{j=1}^{i-1} (1 - \alpha(t_j)) \right) \alpha(t_i). \quad (2)$$

The piecewise-constant function  $h(t_i)$  is an approximation of the rendering probability density function (PDF) to weight the contribution of each sampled point. The opacity value  $\alpha(t_i)$  is computed as  $\alpha(t_i) = 1 - \exp(-\sigma(p_i) \Delta t)$ .



**Explicit Normal Regularization.** To ensure normal consistency on planar surfaces, a normal regularizer  $\mathcal{L}_{\text{normal}}$  is introduced to penalize the deviation of the NeRF-derived surface normal  $\hat{\mathbf{n}}$  from  $\bar{\mathbf{n}}$  defined in Sec. 3.1. We estimate  $\hat{\mathbf{n}}$  in an algebraic manner, using triplets of rays sampled from the plane segment  $\mathcal{M}$  of a local planar primitive  $P$ . More precisely, for each ray triplet  $\mathcal{T} = \{\mathbf{r}_i(t) = \mathbf{o}_c + t\mathbf{v}_i\}_{i=1}^3$  randomly drawn from  $P_a$ , we render its expected termination points  $\{\mathbf{x}_i\}_{i=1}^3$  by eq. (2), and estimate the normal of the plane passing through:

$$\hat{\mathbf{n}} = -\text{sign}(\mathbf{z}^\top \mathbf{v}_1) \cdot \frac{\mathbf{z}}{\|\mathbf{z}\|}, \text{ where } \mathbf{z} = (\mathbf{x}_2 - \mathbf{x}_1) \times (\mathbf{x}_3 - \mathbf{x}_1). \quad (3)$$

Here, the direction of  $\hat{\mathbf{n}}$  is adjusted to point towards the camera (same as  $\bar{\mathbf{n}}_a$ ) by checking the angle between  $\mathbf{z}$  and  $\mathbf{v}_1$ . Then, the normal loss with respect to  $P_a$  is defined as:

$$\mathcal{L}_{\text{normal}}(\sigma; P_a) = \mathbb{E}_{\mathcal{T} \sim P_a} \|\mathbf{1} - \hat{\mathbf{n}}^\top \bar{\mathbf{n}}_a\|_1. \quad (4)$$

**Pseudo-Depth Supervision.** We observe that though the normal regularization induces smoothness in planar regions, it alone is not enough for high geometric accuracy. To further guide the learning process, we introduce *plane-derived pseudo-depth* as extra supervision. The pseudo-depth  $D$  is computed as the distance from the camera centre  $\mathbf{o}_c$  to the corresponding  $P$ :  $D = -(\bar{o} + \bar{\mathbf{n}} \cdot \mathbf{o}_c) / \cos \varphi$ , where  $\varphi$  is the angle between  $\bar{\mathbf{n}}$  and the ray direction  $\mathbf{v}$ . Since defectively estimated  $\bar{\mathbf{n}}$  and  $\bar{o}$  lead to noisy  $D$ , we draw inspiration from DS-NeRF (Deng et al., 2022) to model the depth label of ray  $\mathbf{r}$  as a random variable normally distributed around  $D$  with variance  $\beta^{-1}$ :  $\mathbf{d} \sim \mathcal{N}(t; D, \beta^{-1})$ . For each ray  $\mathbf{r}_i$  drawn from  $P_a$ , we minimize the KL divergence between the pseudo-depth distribution  $\mathcal{N}(t; D_i^a, \beta^{-1})$  and the piecewise-constant rendering PDF  $h_i^a(t)$ :

$$\mathcal{L}_{\text{p-depth}}(\sigma, \bar{\pi}_a; P_a) = \mathbb{E}_{\mathbf{r}_i \sim P_a} D_{\text{KL}}[\mathcal{N}(t; D_i^a, \beta^{-1}) \| h_i^a(t)]. \quad (5)$$

In addition, we enable gradient descent over the estimated plane parameters  $\bar{\pi}_a$  (i.e.,  $\bar{\mathbf{n}}_a$  and  $\bar{o}_a$ ), using gradient signals from  $\mathcal{L}_{\text{p-depth}}$  to jointly optimize the inaccurate local geometry.

### 3.2.2 SEMANTICS BRANCH

As highlighted by AirPlanes (Watson et al., 2024), semantics are crucial in 3D plane reconstruction since ideal planar primitives need to be semantically self-contained. For instance, though geometrically coplanar, a closed door should be regarded as a different planar primitive from the wall that encloses it. However, it is intractable for purely geometric methods, e.g., RANSAC, to resolve such semantic conflicts. To address this, we retrofit the neural field with plane-level semantics.

**Neural Coplanarity Field.** We start by introducing Neural Coplanarity Field (NCF)  $\phi : \mathbb{R}^3 \mapsto \mathbb{R}^d$  that outputs a  $d$ -dimensional feature  $\phi(\mathbf{p})$  over any 3D location  $\mathbf{p}$ . The coplanarity between two rays is defined as the probability that their expected termination points lie on the same plane structure. Here, we aim to measure such coplanarity using the similarity between their rendered features, which we call the *coplanarity feature*:  $\mathbf{f}(\mathbf{x}) = \sum_{i=1}^N h(t_i) \phi(\mathbf{p}_i)$ .

The desired NCF is trained through the margin-based contrastive learning paradigm (Chopra et al., 2005) where the objective comprises two terms: the *intra-primitive* pull loss  $\mathcal{L}_{\text{pull}}$  and the *inter-primitive* push loss  $\mathcal{L}_{\text{push}}$ .

Considering two rays from the same local planar primitive  $P_a$ , e.g.,  $\mathbf{r}_i$  and  $\mathbf{r}_j$ , their coplanarity features constitute a pair of positive samples and are pulled close by minimizing the  $L^2$  distance:

$$\mathcal{L}_{\text{pull}}(\phi; P_a) = \mathbb{E}_{\{\mathbf{r}_i, \mathbf{r}_j\} \sim P_a} \|\mathbf{f}(\mathbf{x}_i) - \mathbf{f}(\mathbf{x}_j)\|_2. \quad (6)$$

Next, we define the *primitive-level* coplanarity feature of  $P_a$  as:  $\bar{\mathbf{f}}_a = \mathbb{E}_{\mathbf{r} \sim P_a} \mathbf{f}(\mathbf{x})$ .  $\mathcal{L}_{\text{push}}$  is computed over these primitive-level features, as we find that this can reduce computation overhead and

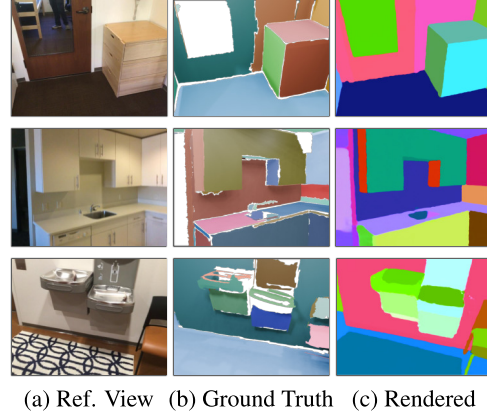


Figure 3: Visualization of NCF.

accelerate convergence. Note that local planar primitives are generated through over-segmentation, and  $\mathcal{L}_{\text{push}}$  is allowed to be computed across images; thereby, two primitives in a batch do not necessarily belong to distinct planar structures. This ambiguity prompts us to incorporate the geometry:  $\bar{\mathbf{f}}_a$  and  $\bar{\mathbf{f}}_b$  form a pair of negative samples only if the estimated plane parameters  $\bar{\pi}_a, \bar{\pi}_b$  are sufficiently far from each other. More formally, the push loss with margin  $m$  is formulated as:

$$\mathcal{L}_{\text{push}}(\phi; P_a, P_b) = \mathbf{1}_{[\|\bar{o}_a - \bar{o}_b\| > t_o \text{ or } \|\bar{\mathbf{n}}_a \cdot \bar{\mathbf{n}}_b\| < t_n]} \cdot \text{ReLU}(m - \|\bar{\mathbf{f}}_a - \bar{\mathbf{f}}_b\|_2), \quad (7)$$

where  $\mathbf{1}_{[\cdot]}$  is the indicator function, and  $t_o, t_n$  are pushing thresholds w.r.t the offset and normal.

As shown in Fig. 3 (c), we visualize the rendered feature maps using PCA (Hastie et al., 2009) to demonstrate what is learned by NCF. The reference views and ground truth are also provided for comparison. The results shows that the proposed NCF can successfully capture the coplanar relationships between different regions with clear boundaries, considering both geometry and semantics.

**Neural Parser.** To obtain instance centroids and subsequently decompose the learned feature field into instances, one can apply unsupervised clustering methods to thousands of rendered features after training (Bhalgat et al., 2023). However, instead of this post-processing, we propose a learning-based module called Neural Parser to concurrently learn a set of *semantic prototypes* during training. Each prototype is assumed to be the centroid of an isotropic Gaussian distributed cluster of coplanarity features, which could be used to represent a semantically isolated subregion.

As illustrated in Fig. 2, we are motivated by NEAT (Xue et al., 2024) to adopt a query-based architecture, where  $N_p$  semantic prototypes  $\{\rho_i \in \mathbb{R}^d\}_{N_p}$  are predicted from  $N_p$  learnable queries  $\{\mathbf{q}_i \in \mathbb{R}^{d_q}\}_{N_p}$  (randomly initialized) through a simple feed-forward network (FFN)  $\theta: \mathbb{R}^{d_q} \mapsto \mathbb{R}^d$ . During each training iteration, the rendered primitive-level features  $\{\bar{\mathbf{f}}\}$  are utilized to supervise the module. Specifically, we first apply DBSCAN (Ester et al., 1996) to these noisy features to obtain  $N_c$  centroids  $\{\mu_i \in \mathbb{R}^d\}_{N_c}$ . Then, the bipartite matching is performed between the predicted prototypes  $\{\rho_i\}_{N_p}$  and centroids  $\{\mu_i\}_{N_c}$  using an efficient Hungarian algorithm (Jonker & Volgenant, 1987). The matching loss is the  $L^2$  norm between each pair. With the optimal permutation of assignment  $\tau$  determined, our objective is to further minimize the distance between the prototypes and their matched centroids:

$$\mathcal{L}_{\text{np}}(\theta, \{\mathbf{q}\}; \{\mu\}) = \sum_{i=1}^{\min(N_p, N_c)} \|\rho_{\tau(i)} - \mu_i\|_2, \quad \rho_{\tau(i)} = \theta(\mathbf{q}_{\tau(i)}). \quad (8)$$

**Overall Training Scheme.** NeuralPlane is trained by assembling all loss terms:

$$\begin{aligned} \mathcal{L} = & \mathcal{L}_{\text{rgb}}(\sigma) + \mathbb{E}_{P_i \sim \mathcal{P}} [\lambda_1 \mathcal{L}_{\text{normal}}(\sigma; P_i) + \lambda_2 \mathcal{L}_{\text{p-depth}}(\sigma, \bar{\pi}_i; P_i) + \lambda_3 \mathcal{L}_{\text{pull}}(\phi; P_i)] \\ & + \mathbb{E}_{\{P_i, P_j\} \sim \mathcal{P}} [\mathcal{L}_{\text{push}}(\phi; P_i, P_j)] + \mathcal{L}_{\text{np}}(\theta, \{\mathbf{q}\}; \{\mu\}), \end{aligned} \quad (9)$$

where  $\mathcal{L}_{\text{rgb}}$  is the standard NeRF photometric loss, and the set  $\mathcal{P}$  denotes all local planar primitives. We set the balancing parameters  $\lambda_1, \lambda_2, \lambda_3$  to 0.01, 0.1 and 0.5, respectively.

### 3.3 EXTRACTING GLOBAL 3D PARAMETRIC PLANES

Once the implicit neural representation is optimized to encode both the geometry and semantics of the scene, a straightforward 3D plane extraction method is employed to make the representation explicit. The process involves five steps: (1) render sufficient termination points and their coplanarity features from training views; (2) assign the label of the nearest semantic prototype to each point based on its rendered coplanarity feature; (3) group these points according to their labels; (4) parametrically fit 3D planes to each point group using RANSAC; (5) project the inliers onto each fitted plane and triangulate the rasterized projection into a mesh, which represents the final planar primitive. We refer the reader to Appendix A.1 for more details.

## 4 EXPERIMENTS

### 4.1 EXPERIMENTAL SETUP

**Datasets.** To evaluate NeuralPlane’s ability to reconstruct 3D plane maps, we conduct experiments on 12 challenging real-world indoor scenes: 8 scenes from ScanNetv2 (Dai et al., 2017) and 4 scenes

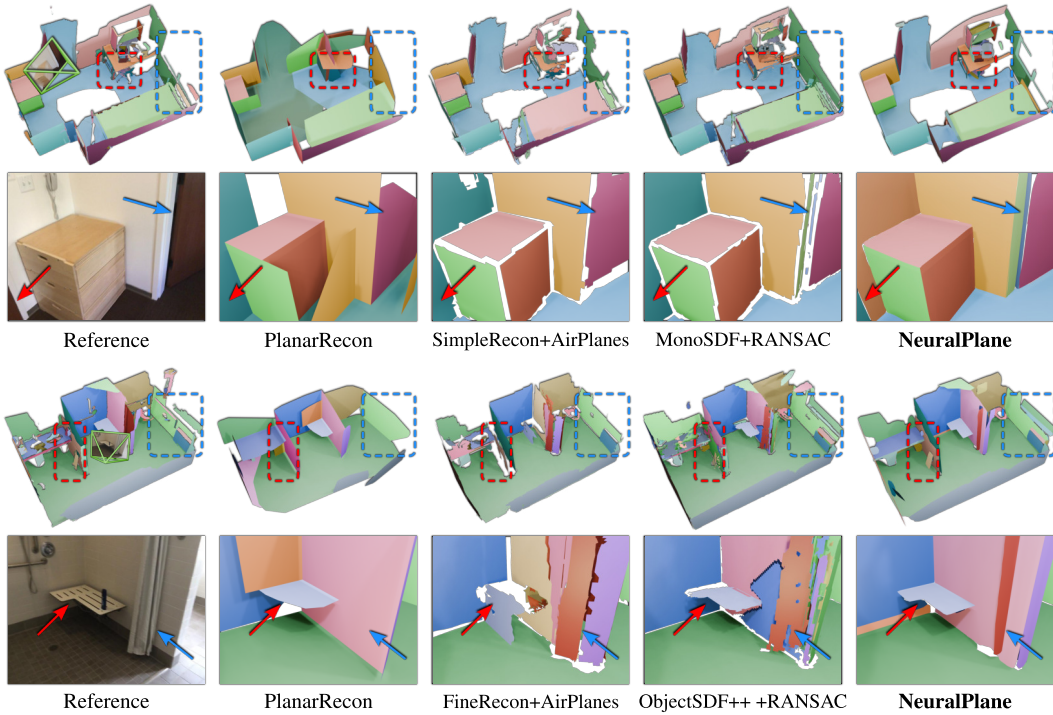


Figure 4: **Qualitative results on ScanNetv2.** For each scene, the first row presents the top view of the entire room, and the second row displays the details viewed from a given pose. Only the best two geometry+RANSAC methods are included for comparison. NeuralPlane reconstructs clean planar structures with fine details and coherent semantics.

from ScanNet++ (Yeshwanth et al., 2023). Following standard practice (Xie et al., 2022), we adopt scripts provided by PlaneRCNN (Liu et al., 2019) to generate ground-truth 3D planes for evaluation.

**Baselines.** Our NeuralPlane is evaluated against the learning-based multi-view plane reconstruction approach PlanarRecon (Xie et al., 2022), as well as a wide variety of geometry+RANSAC methods.

The geometry of the latter is inferred either by learning-based Multi-View Stereo (MVS) methods, including SimpleRecon (Sayed et al., 2022) and FineRecon (Stier et al., 2023), or by representative indoor neural surface reconstruction methods (Wang et al., 2021) listed as follows: (1) ManhattanSDF (Guo et al., 2022), which improves the reconstruction quality by enforcing the Manhattan-world assumption to planar regions like walls and floors; (2) NeurIS (Wang et al., 2022), which utilizes predicted normal priors to adaptively guide the optimization of neural representations; (3) MonoSDF (Yu et al., 2022b), which uses both learned monocular depth and normal priors; (4) ObjectSDF++ (Wu et al., 2023a), which extends MonoSDF by incorporating dense instance annotations for high-fidelity object-compositional surface reconstruction. We also include the traditional surface reconstruction method (Schönberger et al., 2016; Kazhdan & Hoppe, 2013) implemented in COLMAP (Schönberger & Frahm, 2016). Given meshes produced by these methods, we run Sequential RANSAC or its variant, namely AirPlanes (Watson et al., 2024), to partition them into planar primitives. For all data-driven components, we use the official pre-trained models.

**Metrics.** We evaluate the geometric quality of 3D plane reconstruction utilizing standard 3D metrics introduced by Bozic et al. (2021). Among these metrics, we adopt *Chamfer Distance* and *F-score* with a threshold of 5 cm as the comprehensive metrics for comparison. To assess how well the reconstructed planar primitives align with the ground-truth scene semantics, we further employ three conventional segmentation metrics (Arbeláez et al., 2011; Tan et al., 2021; Shi et al., 2023): rand index (RI), variation of information (VOI) and segmentation covering (SC).

**Implementation Details.** NeuralPlane is implemented in Nerfstudio (Tancik et al., 2023) on top of Nerfacto, a unified approach in the literature of NeRF. Considering the lack of texture in typical

Table 1: **Quantitative results on ScanNetv2.** Top-3 results are highlighted as **first**, **second** and **third**. At the top, we also report the quality of raw geometries in 7 baseline methods, using official scene reconstructions as the ground truth. <sup>†</sup> is tested with its MLP variant. <sup>‡</sup> produces a set of semantically decomposed reconstructions, and Seq.RANSAC is executed on each of them independently.

Method	Geometry						Segmentation		
	Accu. ↓	Comp. ↓	Chamfer ↓	Prec. ↑	Recall ↑	F-score ↑	RI ↑	VOI ↓	SC ↑
COLMAP (Schönberger et al., 2016)	18.35	13.40	<b>15.88</b>	40.5	42.4	<b>41.2</b>	-	-	-
SimpleRecon (Sayed et al., 2022)	6.74	5.55	<b>6.15</b>	59.2	58.8	<b>59.0</b>	-	-	-
FineRecon (Stier et al., 2023)	6.12	4.19	<b>5.16</b>	68.6	72.9	<b>70.6</b>	-	-	-
ManhattanSDF (Guo et al., 2022)	9.95	7.51	<b>8.73</b>	50.4	50.9	<b>50.6</b>	-	-	-
NeuRIS (Wang et al., 2022)	10.23	5.69	<b>7.96</b>	62.0	64.8	<b>63.2</b>	-	-	-
MonoSDF <sup>†</sup> (Yu et al., 2022b)	5.28	5.07	<b>5.18</b>	69.7	69.7	<b>69.7</b>	-	-	-
ObjectSDF++ <sup>†</sup> (Wu et al., 2023a)	8.82	5.25	<b>7.03</b>	54.9	68.9	<b>60.9</b>	-	-	-
COLMAP	19.32	13.37	<b>16.34</b>	40.6	40.9	<b>40.6</b>	0.928	3.91	0.154
SimpleRecon	6.24	6.00	<b>6.12</b>	57.7	52.6	<b>54.9</b>	0.949	2.65	0.272
FineRecon	5.20	5.65	<b>5.43</b>	69.1	64.9	<b>66.7</b>	0.941	2.56	0.276
ManhattanSDF +Seq.RANSAC	9.37	8.70	<b>9.04</b>	50.6	51.0	<b>50.8</b>	0.930	2.82	0.281
NeuRIS	9.87	6.35	<b>8.11</b>	59.6	59.3	<b>59.3</b>	0.945	2.57	0.293
MonoSDF	5.91	5.43	<b>5.67</b>	65.9	66.1	<b>65.9</b>	0.945	2.38	0.333
ObjectSDF++ <sup>‡</sup>	8.41	5.35	<b>6.88</b>	58.0	68.8	<b>62.8</b>	0.952	2.32	0.334
SimpleRecon	5.43	6.60	<b>6.01</b>	59.2	51.5	<b>55.1</b>	0.944	2.51	0.341
FineRecon	4.93	5.95	<b>5.44</b>	70.8	62.2	<b>66.2</b>	0.947	2.43	0.310
ManhattanSDF +AirPlanes (Watson et al., 2024)	9.46	9.30	<b>9.38</b>	52.7	50.2	<b>51.3</b>	0.940	2.61	0.315
NeuRIS	6.05	7.38	<b>6.71</b>	66.2	56.7	<b>61.0</b>	0.943	2.55	0.291
MonoSDF	4.57	6.33	<b>5.45</b>	72.2	62.0	<b>66.6</b>	0.948	2.38	0.346
PlanarRecon (Xie et al., 2022)	7.74	11.85	<b>9.80</b>	55.2	44.3	<b>49.0</b>	0.909	3.27	0.265
NeuralPlane@PlaneRecTR	5.38	4.65	<b>5.02</b>	67.6	70.0	<b>68.7</b>	0.949	2.37	0.364
NeuralPlane	4.92	4.27	<b>4.59</b>	70.5	71.9	<b>71.2</b>	0.955	2.25	0.376

indoor scenes, we use the COLMAP toolbox (Sarlin et al., 2019) that supports LoFTR (Sun et al., 2021)<sup>1</sup>, to export adequate 3D keypoints for the initialization of local planar primitives.

We train NeuralPlane for 4k iterations with batches of 8192 rays across all scenes. For the first 1k iterations, we nullify  $\mathcal{L}_{p\text{-depth}}$  and  $\mathcal{L}_{p\text{-push}}$  on local planar primitives that observe fewer than 50 keypoints. After the density field is holistically optimized to a decent state, we re-estimate the plane offsets of these nullified primitives using rendered depth, globally activate the overall loss in eq. (9), and enable the local geometry refinement. We list several key hyperparameters used in our main experiments: the dimension of coplanarity feature  $d = 4$ , the pushing thresholds  $(t_o, t_n) = (8 \text{ cm}, \cos 10^\circ)$ , and the number of semantic prototypes  $N_p = 32$ . A fixed set of hyperparameters is employed across all test scenes. Preprocessing local planar primitives takes around 2 to 5 minutes, followed by about 6 minutes for training on a single NVIDIA RTX 3090 GPU.

## 4.2 EVALUATION

**ScanNetv2.** We select 8 challenging scenes with diverse layouts to benchmark the adaptability of various methods. To demonstrate the superiority of our local planar primitives generation method introduced in Sec. 3.1, we include a variant denoted by *NeuralPlane@PlaneRecTR*, where the initial local planar primitives are instead produced by PlaneRecTR (Shi et al., 2023). As reported in Tab. 1, NeuralPlane excels existing methods across all metrics. For geometry+RANSAC methods, we observe that AirPlanes (Watson et al., 2024) in combination with FineRecon (Stier et al., 2023) or MonoSDF (Yu et al., 2022b) exhibits impressive results in Precision but suffers a significant drop in Recall. This indicates that incorporating learned plane embeddings can effectively avoid the undesirable fusion of adjacent planes and thus better fit the input geometry (high precision). However, the involvement of plane embeddings during RANSAC also incurs the risk of missing planes, resulting in more false negatives (low recall). In contrast, NeuralPlane strikes a good balance between Precision and Recall. In addition, we observe that independently applying RANSAC to each decomposed mesh of ObjectSDF++, which is optimized with *ground-truth instance annotations*, yields improved geometry and segmentation. However, NeuralPlane achieves even better segmentation with only *machine-predicted* masks. See Fig. 4 for qualitative evaluation.

<sup>1</sup>a transformer-based dense matcher pretrained on a large dataset of internet photos (Li & Snavely, 2018).



Table 2: **Quantitative results on ScanNet++**. Top-3 results are highlighted as **first**, **second** and **third**. <sup>†</sup> is tested using its Multi-Res Grids variant.

Method	Geometry						Segmentation		
	Accu. ↓	Comp. ↓	Chamfer ↓	Prec. ↑	Recall ↑	F-score ↑	RI ↑	VOI ↓	SC ↑
COLMAP	24.42	14.53	<b>19.47</b>	47.4	44.2	<b>45.4</b>	0.920	3.91	0.160
SimpleRecon	11.03	8.54	<b>9.79</b>	43.9	45.8	<b>44.6</b>	0.936	3.17	0.195
FineRecon	4.70	6.03	<b>5.36</b>	80.3	71.1	<b>75.3</b>	0.929	2.79	0.252
ManhattanSDF	8.72	8.67	<b>8.70</b>	59.4	56.3	<b>57.7</b>	0.928	3.06	0.248
NeuRIS	5.35	<b>4.33</b>	<b>4.84</b>	81.4	<b>80.4</b>	<b>80.9</b>	<b>0.941</b>	<b>2.46</b>	<b>0.315</b>
MonoSDF <sup>†</sup>	5.59	<b>4.60</b>	<b>5.09</b>	77.0	<b>78.5</b>	<b>77.7</b>	0.939	<b>2.47</b>	<b>0.288</b>
SimpleRecon	7.97	9.84	<b>8.91</b>	46.5	42.1	<b>44.1</b>	0.931	2.90	0.219
FineRecon	<b>3.21</b>	7.54	<b>5.37</b>	<b>84.0</b>	68.7	<b>75.5</b>	<b>0.941</b>	2.66	0.277
ManhattanSDF	7.35	9.84	<b>8.59</b>	57.9	52.0	<b>54.5</b>	0.935	2.85	0.267
NeuRIS	<b>2.99</b>	6.38	<b>4.69</b>	<b>87.3</b>	73.8	<b>79.9</b>	<b>0.943</b>	2.53	0.287
MonoSDF <sup>†</sup>	<b>3.21</b>	7.38	<b>5.29</b>	<b>82.8</b>	67.6	<b>74.2</b>	0.935	2.69	0.264
PlanarRecon	7.91	20.67	<b>14.29</b>	53.1	38.0	<b>43.8</b>	0.900	3.49	0.231
NeuralPlane@PlaneRecTR	6.03	6.31	<b>6.17</b>	71.1	69.1	<b>70.0</b>	0.939	2.72	0.301
NeuralPlane	<b>4.33</b>	<b>4.87</b>	<b>4.60</b>	80.8	<b>78.7</b>	<b>79.7</b>	<b>0.950</b>	<b>2.38</b>	<b>0.356</b>

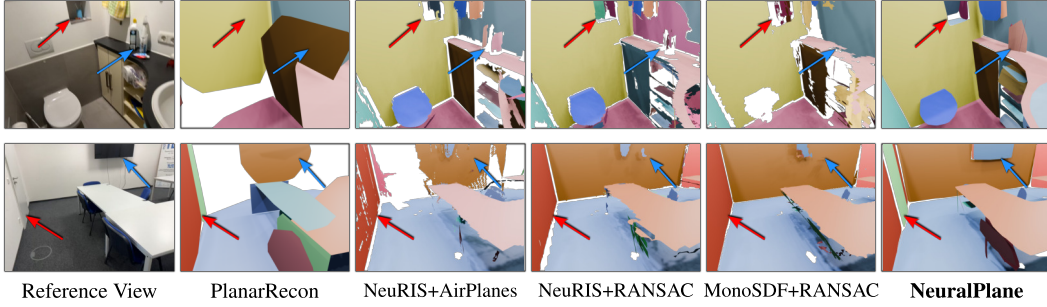


Figure 5: **3D plane reconstruction results on ScanNet++**.

**ScanNet++**. We further conduct experiments on 4 scenes from the newly released ScanNet++ (Yeshwanth et al., 2023), ensuring that no pre-trained model adopted in our method or baselines has encountered similar scene layouts before. These scenes are challenging due to the significant absence of textures. We observe that low-texture regions generate normal priors that provide NeuRIS with relatively precise geometry guidance, but result in sparse and misleading SfM keypoints for our method. Despite this, as reported in Tab. 2, our approach still achieves competitive geometric performance. Moreover, our method consistently demonstrates remarkable segmentation performance, preserving fine-grained and coherent semantics (see qualitative results in Fig. 5). It is also worth noting that in our method, geometry is directly represented by volume density, which allows for a 40× training speedup compared to other neural implicit methods. A more detailed comparison of reconstruction efficiency is provided in Appendix A.4.

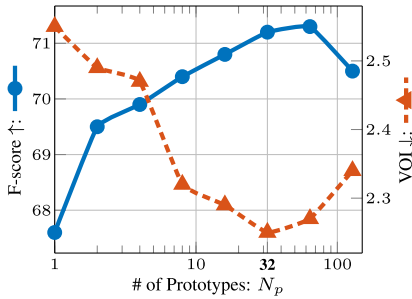
Table 3: **Ablation study on proposed components**. NCF and NP denote the proposed neural coplanarity field and neural parser module, respectively. The best results are in **bold**.

Method	Components					Geometry		Segmentation		
	$\mathcal{L}_{\text{normal}}$	$\mathcal{L}_{\text{p-depth}}$	Refine.	NCF	NP	Chamfer ↓	F-score ↑	RI ↑	VOI ↓	SC ↑
Nerfacto	-	-	-	-	-	19.61	17.3	0.903	4.66	0.119
Model A	-	✓	✓	✓	✓	4.96	68.1	0.951	2.27	0.371
Model B	✓	-	✓	✓	✓	10.01	41.9	0.935	2.98	0.305
Model C	✓	✓	-	✓	✓	5.02	66.0	0.944	2.44	0.358
Model D	✓	✓	✓	-	-	4.98	66.1	0.940	2.59	0.352
Model E	✓	✓	✓	✓	-	4.91	69.8	0.947	2.40	0.364
NeuralPlane	✓	✓	✓	✓	✓	<b>4.59</b>	<b>71.2</b>	<b>0.955</b>	<b>2.25</b>	<b>0.376</b>

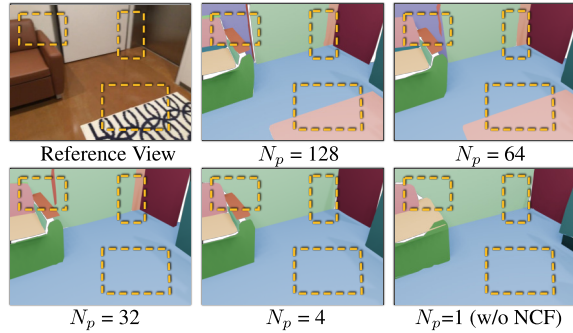
### 4.3 ABLATION STUDY

**Ablating Components.** To verify the merits of each component in NeuralPlane, we conduct ablations using the 8 scenes from ScanNetv2. Quantitative results are listed in Tab. 3, where Nerfacto is our backbone with default settings and in Model E, the neural parser is replaced by post-clustering similar to ContrastiveLift (Bhalgat et al., 2023). Nerfacto and models A through C all struggle with degraded reconstruction quality due to insufficient geometric guidance. Model D disregards high-level semantics during the plane extraction, resulting in significant semantic conflicts as depicted in Fig. 6 (d). NeuralPlane excels all these models on all metrics, demonstrating that geometry and semantics are tightly entangled in the task, and that the combination in our method appears notable synergy.

**Ablating Number of Semantic Prototypes.** Remember that the number of semantic prototypes  $N_p$  is a heuristically determined hyperparameter in neural parser and we opt for  $N_p = 32$  across all scenes in our main experiments. We assess the effect of varying  $N_p$  on the reconstruction results and observe that both geometry and segmentation deteriorate as  $N_p$  continues to increase (see Fig. 7 (a)). This could be explained by the inherent ambiguity in defining what constitutes a single plane structure: in Fig. 7 (b), we illustrate that by controlling  $N_p$ , one can adjust the level of detail (LOD), while the level with  $N_p = 32$  is potentially closer to the ground truth used for evaluation.



(a) Number of Semantic Prototypes



(b) Different Levels of Detail

Figure 7: **Ablation study on number of semantic prototypes.** (a) There is a minor decline in performance as  $N_p$  grows. (b) A case shows that the level of detail is controlled by  $N_p$ .

## 5 CONCLUSION

Reconstructing man-made environments as arrangements of planar primitives demands not only geometric fidelity but also semantic alignment. In this paper, we introduced NeuralPlane, a novel plane reconstruction pipeline that learns accurate 3D locations and instance-level semantics of plane structures from multi-view plane observations implicitly using neural fields. We presented an annotation-free module that incorporates strong single image priors to identify well-defined 2D plane segments, and demonstrated how these segments can drive the joint modeling of scene geometry and semantics. Our method achieves remarkable performance in delivering high-quality planar primitives with fine details and coherent semantics. Besides, our approach shows the potential in adjusting the level of detail, which we believe is practical and will provide inspiration for future research.

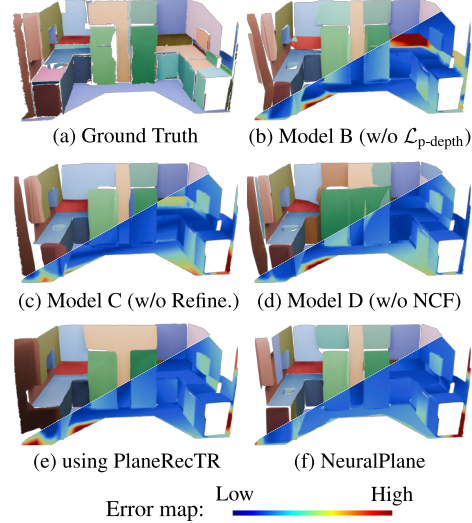


Figure 6: **Qualitative ablation on components.** The upper part shows the reconstructed 3D planes in different colors. The lower part presents the error map.

## REFERENCES

- Samir Agarwala, Linyi Jin, Chris Rockwell, and David F. Fouhey. PlaneFormers: From sparse view planes to 3D reconstruction. In *ECCV*, pp. 192–209. 2022. 3
- Pablo Arbeláez, Michael Maire, Charless C. Fowlkes, and Jitendra Malik. Contour detection and hierarchical image segmentation. *IEEE Trans. Pattern Anal. Mach. Intell.*, 33(5):898–916, 2011. 7, 18
- ARCore. Fundamental Concepts: Environmental Understanding. In *Google for Developer: Augmented Reality Essentials*, Accessed: 2024-08-23. 1
- ARKit. Placing content on detected planes. In *Apple Developer Documentation*, Accessed: 2024-08-23. 1
- Eduardo Arnold, Jamie Wynn, Sara Vicente, Guillermo Garcia-Hernando, Áron Monszpart, Victor Adrian Prisacariu, Daniyar Turmukhambetov, and Eric Brachmann. Map-free visual relocalization: Metric pose relative to a single image. In *ECCV*, pp. 690–708, 2022. 20
- Gwangbin Bae, Ignas Budvytis, and Roberto Cipolla. Estimating and Exploiting the Aleatoric Uncertainty in Surface Normal Estimation. In *ICCV*, pp. 13117–13126, 2021. 3
- Yash Sanjay Bhargat, Iro Laina, Joao F. Henriques, Andrea Vedaldi, and Andrew Zisserman. Contrastive lift: 3D object instance segmentation by slow-fast contrastive fusion. In *NeurIPS*, 2023. 3, 6, 10, 19
- Aljaz Bozic, Pablo Palafox, Justus Thies, Angela Dai, and Matthias Niessner. TransformerFusion: Monocular RGB scene reconstruction using transformers. In *NeurIPS*, 2021. 7
- Zheng Chen, Qingan Yan, Huangying Zhan, Changjiang Cai, Xiangyu Xu, Yuzhong Huang, Weihang Wang, Ziyue Feng, Lantao Liu, and Yi Xu. PlanarNeRF: Online Learning of Planar Primitives with Neural Radiance Fields, *arXiv preprint arXiv:2401.00871*, 2023. 3
- Sumit Chopra, Raia Hadsell, and Yann LeCun. Learning a similarity metric discriminatively, with application to face verification. In *CVPR*, pp. 539–546, 2005. 5
- Angela Dai, Angel X. Chang, Manolis Savva, Maciej Halber, Thomas Funkhouser, and Matthias Nießner. ScanNet: Richly-annotated 3D reconstructions of indoor scenes. In *CVPR*, pp. 5828–5839, 2017. 6, 17
- Kangle Deng, Andrew Liu, Jun-Yan Zhu, and Deva Ramanan. Depth-supervised NeRF: Fewer Views and Faster Training for Free. In *CVPR*, pp. 12882–12891. 2022. 5, 16
- Daniel DeTone, Tomasz Malisiewicz, and Andrew Rabinovich. SuperPoint: Self-supervised interest point detection and description. In *CVPRW*, pp. 224–236. 2018. 20
- Johan Edstedt, Qiyu Sun, Georg Bökman, Mårten Wadenbäck, and Michael Felsberg. RoMa: Robust dense feature matching. In *CVPR*, pp. 19790–19800, 2024. 20
- Martin Ester, Hans-Peter Kriegel, Jörg Sander, and Xiaowei Xu. A density-based algorithm for discovering clusters in large spatial databases with noise. In *KDD*, pp. 226–231. 1996. 6
- Zhiwen Fan, Peihao Wang, Yifan Jiang, Xinyu Gong, Dejia Xu, and Zhangyang Wang. NeRF-SOS: Any-view self-supervised object segmentation on complex scenes. In *ICLR*. 2023. 3
- Martin A. Fischler and Robert C. Bolles. Random sample consensus: A paradigm for model fitting with applications to image analysis and automated cartography. *Communications of The Acm*, 24(6):381–395, 1981. 1
- Haoyu Guo, Sida Peng, Haotong Lin, Qianqian Wang, Guofeng Zhang, Hujun Bao, and Xiaowei Zhou. Neural 3D scene reconstruction with the manhattan-world assumption. In *CVPR*, pp. 5511–5520, 2022. 7, 8, 20
- T. Hastie, R. Tibshirani, and J.H. Friedman. *The Elements of Statistical Learning: Data Mining, Inference, and Prediction*, volume 2. Springer, 2009. 6

- Linyi Jin, Shengyi Qian, Andrew Owens, and David F. Fouhey. Planar surface reconstruction from sparse views. In *ICCV*, pp. 12971–12980. 2021. 3
- R. Jonker and A. Volgenant. A shortest augmenting path algorithm for dense and sparse linear assignment problems. *Computing*, 38(4):325–340, 1987. 6
- Michael Kazhdan and Hugues Hoppe. Screened poisson surface reconstruction. *ACM Trans. Graph.*, 32(3):29:1–29:13, 2013. 7
- Justin Kerr, Chung Min Kim, Ken Goldberg, Angjoo Kanazawa, and Matthew Tancik. LERF: Language embedded radiance fields. In *ICCV*, pp. 19672–19682. 2023. 3
- Chung Min Kim, Mingxuan Wu, Justin Kerr, Ken Goldberg, Matthew Tancik, and Angjoo Kanazawa. GARField: Group Anything with Radiance Fields. In *CVPR*, pp. 21530–21539. 2024. 1, 3, 17
- Alexander Kirillov, Eric Mintun, Nikhila Ravi, Hanzi Mao, Chloe Rolland, Laura Gustafson, Tete Xiao, Spencer Whitehead, Alexander C. Berg, Wan-Yen Lo, Piotr Dollár, and Ross Girshick. Segment Anything. In *ICCV*, pp. 3992–4003. 2023. 3, 15
- Florian Kluger, Eric Brachmann, Michael Ying Yang, and Bodo Rosenhahn. Robust shape fitting for 3D scene abstraction. *IEEE Trans. Pattern Anal. Mach. Intell.*, 46(9):6306–6325, 2024. 1
- Sosuke Kobayashi, Eiichi Matsumoto, and Vincent Sitzmann. Decomposing NeRF for editing via feature field distillation. In *NeurIPS*, 2022. 3
- Lei Li, Songyou Peng, Zehao Yu, Shaohui Liu, Rémi Pautrat, Xiaochuan Yin, and Marc Pollefeys. 3D neural edge reconstruction. In *CVPR*, pp. 21219–21229, 2024. 1, 3
- Zhengqi Li and Noah Snavely. MegaDepth: Learning single-view depth prediction from internet photos. In *CVPR*, pp. 2041–2050, 2018. 8
- Philipp Lindenberger, Paul-Edouard Sarlin, and Marc Pollefeys. LightGlue: Local feature matching at light speed. In *ICCV*, pp. 17581–17592. 2023. 20
- Chen Liu, Kihwan Kim, Jinwei Gu, Yasutaka Furukawa, and Jan Kautz. PlaneRCNN: 3D plane detection and reconstruction from a single image. In *CVPR*, pp. 4445–4454. 2019. 3, 7, 17
- Jiacheng Liu, Pan Ji, Nitin Bansal, Changjiang Cai, Qingan Yan, Xiaolei Huang, and Yi Xu. PlaneMVS: 3D plane reconstruction from multi-view stereo. In *CVPR*, pp. 8655–8665, 2022. 3
- Zheng Liu, Xiyuan Liu, and Fu Zhang. Efficient and consistent bundle adjustment on lidar point clouds. *IEEE Trans. Robotics*, 39(6):4366–4386, 2023. 1
- Stuart P. Lloyd. Least squares quantization in PCM. *IEEE Trans. Inf. Theory*, 28(2):129–136, 1982. 3
- Hidenobu Matsuki, Riku Murai, Paul H. J. Kelly, and Andrew J. Davison. Gaussian Splatting SLAM. In *CVPR*, 2024. 20
- Kirill Mazur, Gwangbin Bae, and Andrew J. Davison. SuperPrimitive: Scene Reconstruction at a Primitive Level. In *CVPR*, pp. 4979–4989, 2024. 1
- Marina Meila. Comparing clusterings: An axiomatic view. In *ICML*, pp. 577–584. 2005. 18
- Ben Mildenhall, Pratul P. Srinivasan, Matthew Tancik, Jonathan T. Barron, Ravi Ramamoorthi, and Ren Ng. NeRF: Representing Scenes as Neural Radiance Fields for View Synthesis. In *ECCV*, pp. 405–421. 2020. 4
- Zak Murez, Tarrence van As, James Bartolozzi, Ayan Sinha, Vijay Badrinarayanan, and Andrew Rabinovich. Atlas: End-to-end 3D scene reconstruction from posed images. In *ECCV*, pp. 414–431. 2020. 1



- Liangliang Nan and Peter Wonka. PolyFit: Polygonal surface reconstruction from point clouds. In *ICCV*, pp. 2372–2380. 2017. [20](#)
- Minyoung Park, Mirae Do, YeonJae Shin, Jaeseok Yoo, Jongkwang Hong, Joongrock Kim, and Chul Lee. H2O-SDF: Two-phase Learning for 3D Indoor Reconstruction using Object Surface Fields. In *ICLR*, 2024. [3](#), [19](#)
- Paul-Edouard Sarlin, Cesar Cadena, Roland Siegwart, and Marcin Dymczyk. From Coarse to Fine: Robust Hierarchical Localization at Large Scale. In *CVPR*, pp. 12708–12717. 2019. [8](#)
- Mohamed Sayed, John Gibson, Jamie Watson, Victor Prisacariu, Michael Firman, and Clément Godard. SimpleRecon: 3D reconstruction without 3D convolutions. In *ECCV*, pp. 1–19, 2022. [3](#), [7](#), [8](#), [17](#)
- Johannes L. Schönberger, Enliang Zheng, Jan-Michael Frahm, and Marc Pollefeys. Pixelwise view selection for unstructured multi-view stereo. In *ECCV*, pp. 501–518. 2016. [1](#), [7](#), [8](#)
- Johannes Lutz Schönberger and Jan-Michael Frahm. Structure-from-motion revisited. In *CVPR*, pp. 4104–4113, 2016. [7](#)
- Jingjia Shi, Shuaifeng Zhi, and Kai Xu. PlaneRecTR: Unified Query Learning for 3D Plane Recovery from a Single View. In *ICCV*, pp. 9377–9386, 2023. [3](#), [7](#), [8](#), [15](#)
- Noah Stier, Anurag Ranjan, Alex Colburn, Yajie Yan, Liang Yang, Fangchang Ma, and Baptiste Angles. FineRecon: Depth-aware Feed-forward Network for Detailed 3D Reconstruction. In *ICCV*, pp. 18423–18432. 2023. [7](#), [8](#), [17](#)
- Jia Ming Sun, Ze Hong Shen, Yuang Wang, Hu Jun Bao, and Xiao Wei Zhou. LoFTR: Detector-Free Local Feature Matching with Transformers. In *CVPR*, pp. 8918–8927. 2021. [8](#), [20](#)
- Bin Tan, Nan Xue, Song Bai, Tianfu Wu, and Gui-Song Xia. PlaneTR: Structure-Guided Transformers for 3D Plane Recovery. In *ICCV*, pp. 4186–4195, 2021. [3](#), [7](#)
- Bin Tan, Nan Xue, Tianfu Wu, and Gui-Song Xia. NOPE-SAC: Neural one-plane RANSAC for sparse-view planar 3D reconstruction. *IEEE Trans. Pattern Anal. Mach. Intell.*, 45(12):15233–15248, 2023. [3](#)
- Matthew Tancik, Ethan Weber, Evonne Ng, Ruilong Li, Brent Yi, Justin Kerr, Terrance Wang, Alexander Kristoffersen, Jake Austin, Kamyar Salahi, Abhik Ahuja, David McAllister, and Angjoo Kanazawa. Nerfstudio: A Modular Framework for Neural Radiance Field Development. In *ACM SIGGRAPH*, pp. 1–12, 2023. [7](#)
- Bing Wang, Lu Chen, and Bo Yang. DM-NeRF: 3D scene geometry decomposition and manipulation from 2D images. In *ICLR*. 2023. [3](#)
- Jiepeng Wang, Peng Wang, Xiaoxiao Long, Christian Theobalt, Taku Komura, Lingjie Liu, and Wenping Wang. NeuRIS: Neural Reconstruction of Indoor Scenes Using Normal Priors. In *ECCV*, pp. 139–155. 2022. [7](#), [8](#), [19](#), [20](#)
- Peng Wang, Lingjie Liu, Yuan Liu, Christian Theobalt, Taku Komura, and Wenping Wang. NeuS: Learning neural implicit surfaces by volume rendering for multi-view reconstruction. In *NeurIPS*, 2021. [7](#)
- Jamie Watson, Filippo Aleotti, Mohamed Sayed, Zawar Qureshi, Oisin Mac Aodha, Gabriel Brostow, Michael Firman, and Sara Vicente. AirPlanes: Accurate plane estimation via 3D-consistent embeddings. In *CVPR*, pp. 5270–5280, 2024. [1](#), [2](#), [3](#), [5](#), [7](#), [8](#), [18](#), [19](#)
- Qianyi Wu, Kaisiyuan Wang, Kejie Li, Jianmin Zheng, and Jianfei Cai. ObjectSDF++: Improved Object-Compositional Neural Implicit Surfaces. In *ICCV*, pp. 21707–21717. 2023a. [7](#), [8](#)
- Tong Wu, Jiaqi Wang, Xingang Pan, Xudong XU, Christian Theobalt, Ziwei Liu, and Dahua Lin. Voxurf: Voxel-based efficient and accurate neural surface reconstruction. In *ICLR*, 2023b. [1](#)

- Yiming Xie, Matheus Gadelha, Fengting Yang, Xiaowei Zhou, and Huaizu Jiang. PlanarRecon: Realtime 3D Plane Detection and Reconstruction from Posed Monocular Videos. In *CVPR*, pp. 6209–6218, 2022. 1, 2, 3, 7, 8, 18
- Nan Xue, Bin Tan, Yuxi Xiao, Liang Dong, Gui-Song Xia, Tianfu Wu, and Yujun Shen. NEAT: Distilling 3D Wireframes from Neural Attraction Fields. In *CVPR*, pp. 19968–19977. 2024. 1, 3, 6
- Bangbang Yang, Yinda Zhang, Yinghao Xu, Yijin Li, Han Zhou, Hujun Bao, Guofeng Zhang, and Zhaopeng Cui. Learning object-compositional neural radiance field for editable scene rendering. In *ICCV*, pp. 13759–13768. 2021. 3
- Fengting Yang and Zihan Zhou. Recovering 3D planes from a single image via convolutional neural networks. In *ECCV*, pp. 87–103, 2018. 3
- Yunfan Ye, Renjiao Yi, Zhirui Gao, Chenyang Zhu, Zhiping Cai, and Kai Xu. NEF: Neural edge fields for 3D parametric curve reconstruction from multi-view images. In *CVPR*, pp. 8486–8495. 2023. 1, 3
- Chandan Yeshwanth, Yueh-Cheng Liu, Matthias Nießner, and Angela Dai. ScanNet++: A high-fidelity dataset of 3D indoor scenes. In *ICCV*, pp. 12–22, 2023. 7, 9, 17
- Haiyang Ying, Yixuan Yin, Jinzhi Zhang, Fan Wang, Tao Yu, Ruqi Huang, and Lu Fang. OmniSeg3D: Omniversal 3D Segmentation via Hierarchical Contrastive Learning. In *CVPR*, pp. 20612–20622. 2024. 1
- Hong-Xing Yu, Leonidas J. Guibas, and Jiajun Wu. Unsupervised discovery of object radiance fields. In *ICLR*. 2022a. 3
- Mulin Yu and Florent Lafarge. Finding good configurations of planar primitives in unorganized point clouds. In *CVPR*, pp. 6357–6366. 2022. 1, 18
- Zehao Yu, Jia Zheng, Dongze Lian, Zihan Zhou, and Shenghua Gao. Single-image piece-wise planar 3D reconstruction via associative embedding. In *CVPR*, pp. 1029–1037. 2019. 3
- Zehao Yu, Songyou Peng, Michael Niemeyer, Torsten Sattler, and Andreas Geiger. MonoSDF: Exploring Monocular Geometric Cues for Neural Implicit Surface Reconstruction. In *NeurIPS*. 2022b. 7, 8, 17, 19, 20
- Kai Zhang, Gernot Riegler, Noah Snavely, and Vladlen Koltun. NeRF++: Analyzing and improving neural radiance fields, *arXiv preprint arXiv:2010.07492*, 2020. 4
- Lipu Zhou, Shengze Wang, and Michael Kaess.  $\pi$ -LSAM: LiDAR smoothing and mapping with planes. In *ICRA*, pp. 5751–5757, 2021. 1
- Zi Han Zhu, Songyou Peng, Viktor Larsson, Wei Wei Xu, Hu Jun Bao, Zhao Peng Cui, Martin R. Oswald, and Marc Pollefeys. NICE-SLAM: Neural Implicit Scalable Encoding for SLAM. In *CVPR*, pp. 12776–12786. 2022. 20

## A APPENDIX

In Appendix A.1, we first provide additional details about the method, including the procedures of generating 2D plane segments and extracting 3D parametric planes. Next, we present further implementation details, including the network architecture and training configurations (Appendix A.2). Then, detailed descriptions on the data processing steps, implementation details of baseline methods and the evaluation protocol are provided in Appendix A.3. More experimental evaluation and qualitative results can be found in Appendix A.4. Finally, in Appendix A.5, we discuss the limitations of our method and anticipate future research trajectories.

### A.1 ADDITIONAL METHOD DETAILS

**2D Plane Segments from Monocular Priors.** In Sec. 3.1, when identifying plane regions from a single image, we first apply K-means clustering ( $K=8$ ) to its estimated normal map, and select the largest 6 clusters as initial masks (see Fig. 8 (c)), assuming they correspond to low-frequency regions. We then utilize the zero-shot capacities of the Segment Anything Model (SAM) to generate all possible plane instances by prompting with 256 query points evenly sampled from the initial masks. SAM-generated masks are filtered using post-processing techniques including stability checks and non-maximal suppression (NMS) introduced by Kirillov et al. (2023). After eliminating unstable and duplicate masks, we retain only the smallest mask for each query. The overlaps between the SAM-generated masks and the initial masks, expected to be geometrically continuous and smooth, represent the desired 2D plane segments (see Fig. 8 (d)). We further remove noisy 2D plane segments whose pixel areas are less than 0.4 % of the image size.

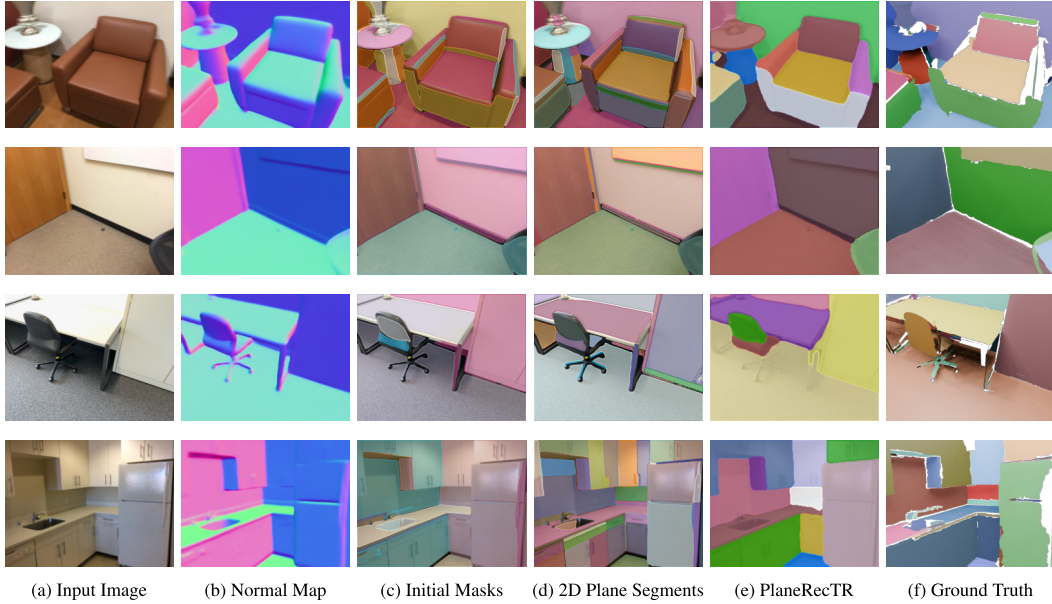


Figure 8: **2D plane segment generation.** We cluster (b) monocular normal priors for (c) initial masks, and then enforce geometric continuity by semantic over-segmentation for (d) 2D plane segments. (e) Single-view plane segmentation results by PlaneRecTR (Shi et al., 2023). (f) Ground truth rendered from 3D plane annotations.

Compared to the PlaneRecTR’s predictions in Fig. 8 (e) and the ground truth in Fig. 8 (f), our method exhibits over-segmentation; in other words, it tends to split a single plane into multiple segments due to SAM’s fine-grained visual understanding capability.

**Pseudo-Depth Supervision.** In Sec. 3.2.1, *plane-derived pseudo-depth* is introduced as extra regularization. The expected pseudo-depth  $D$  of a ray  $\mathbf{r}$  originated from local planar primitive  $P$  is computed base on the estimated plane parameters  $\bar{\pi} = [\bar{\mathbf{n}}, \bar{o}]$  (defined in world space). More precisely, let the expected termination point of  $\mathbf{r}$  be denoted by  $\mathbf{x} = \mathbf{o}_c + D\mathbf{v}$ , where  $\mathbf{o}_c$  is the camera center and  $\mathbf{v}$  is the unit direction vector. Since  $\mathbf{r}$  is assumed to terminate at the planar surface  $\bar{\pi}$ , we

have

$$\bar{\mathbf{n}} \cdot (\mathbf{o}_c + D\mathbf{v}) + \bar{o} = 0, \quad (10)$$

which can be rewritten as

$$D = \frac{-(\bar{o} + \bar{\mathbf{n}} \cdot \mathbf{o}_c)}{\langle \bar{\mathbf{n}}, \mathbf{v} \rangle} = \frac{-(\bar{o} + \bar{\mathbf{n}} \cdot \mathbf{o}_c)}{\cos \varphi}, \quad (11)$$

where  $\varphi$  is the angle between  $\bar{\mathbf{n}}$  and  $\mathbf{v}$ .

Motivated by DS-NeRF (Deng et al., 2022), the pseudo-depth loss defined in eq. (5) encourages the termination distribution of a ray to match the pseudo-depth distribution. Different from the paper, we allow gradients to flow through the pseudo-depth distribution, thereby jointly optimizing  $\bar{\mathbf{n}}$  and  $\bar{o}$ . Here, the KL divergence is computed as:

$$D_{\text{KL}} [\mathcal{N}(t; D, \beta^{-1}) \| \mathbf{h}(t)] = \int \mathcal{N}(t; D, \beta^{-1}) \log \left[ \frac{\mathcal{N}(t; D, \beta^{-1})}{\mathbf{h}(t)} \right] dt \quad (12)$$

$$\approx \sum_j \mathcal{N}(t_j; D, \beta^{-1}) \log \left[ \frac{\mathcal{N}(t_j; D, \beta^{-1})}{\mathbf{h}(t_j)} \right] \Delta t_j, \quad (13)$$

where  $\mathcal{N}(t; D, \beta^{-1})$  denotes the normal distribution that are used to model the noisy pseudo-depth variable  $d$ , and  $\mathbf{h}(t)$  is the piecewise-constant approximation of the rendering probability density function defined in eq. (2). Then, we have:

$$\begin{aligned} D_{\text{KL}} [\mathcal{N}(t; D, \beta^{-1}) \| \mathbf{h}(t)] \\ \propto \sum_j \exp \left( -\frac{\beta(t_j - D)^2}{2} \right) \left( \log \sqrt{\frac{\beta}{2\pi}} - \frac{\beta(t_j - D)^2}{2} - \log \mathbf{h}(t_j) \right) \Delta t_j. \end{aligned} \quad (14)$$

The variance parameter  $\beta^{-1}$  is fixed to 0.005 across all rays.

**3D Parametric Plane Extraction.** After the training is completed, in Sec. 3.3, we design a straight-forward algorithm to extract 3D parametric planes from the learned neural representation. More specifically, for a given local planar primitive  $P$ , we randomly sample 128 rays from its 2D plane segment and render their termination points. The normal of  $P$  is also assigned to each termination point as its local normal. To render the coplanarity features more efficiently, instead of sampling and integrating features along the rays, we simply use features queried at the termination locations as the ray-level coplanarity features. To group these termination points into different subregions, we first find the closest semantic prototype to each coplanarity feature by measuring the Euclidean distance in feature space. If more than half of the features share the same nearest semantic prototype, then we assign the label of that prototype to all the points. Otherwise, this local planar primitive is considered ambiguous and discarded as an outlier. We continue sampling until the number of successfully labeled points exceeds  $2 \times 10^6$ .

After grouping these points by their labels, we sequentially fit 3D planes to each group using RANSAC. A point is considered an inlier if: (1) the angle between its normal and the normal hypothesis is less than  $20^\circ$ , and (2) the distance from the point to the plane is less than 0.08 m.

Next, given a collection of fitted plane parameters and inliers, we can transform them into triangulated planar surfaces by:

- (1) Downsample the inliers using voxel grid filtering with a leaf size of 1 cm.
- (2) Project the downsampled points onto the fitted plane and rasterize the 2D projection map into a regular binary grid with a resolution of 2 cm.
- (3) Traverse the binary grid and triangulate by connecting occupied neighbors, which produces a 2D mesh.
- (4) Backproject the 2D mesh into the original 3D space to obtain a 3D mesh that represents a real-world planar structure.



## A.2 ADDITIONAL IMPLEMENTATION DETAILS

**Network Architecture.** The neural coplanarity field is configured as a separate output head alongside the default Nerf model (see Fig. 9). The coplanarity features are encoded by a 12-level hashgrid with resolutions sampled from 16 to 256, and a 4-layer MLP with hidden dimensions of 256 and ReLU activation. To speed up the training process, we follow GARField (Kim et al., 2024) to first render the hash value and then feed it into the coplanarity feature MLP. In addition, we constrain coplanarity features to a unit hypersphere. The feed-forward network  $\theta$  employed in Neural Parser is a 3-layer MLP with both input and hidden dimensions of 8 and ReLU activation.

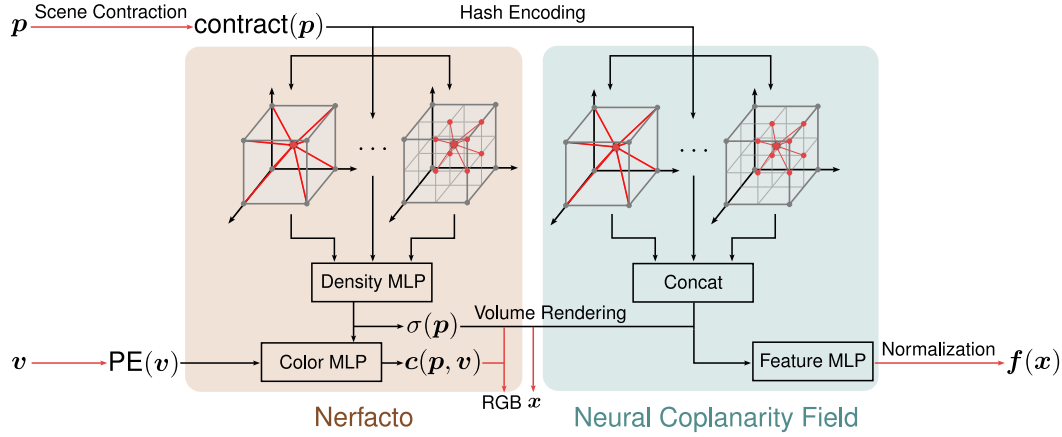


Figure 9: Network architecture.

**Training Details.** Before training, camera poses are centralized without scale adjustment, and we disable joint pose optimization using the provided poses. During each training iteration, we randomly select 128 local planar primitives with probabilities weighted by the sizes of corresponding 2D plane segments. In each local planar primitive, we uniformly sample  $n = 8192 / 128 = 64$  rays, with  $N=48$  points sampled per ray. We further randomly generate 64 triplets and 64 pairs of rays to obtain explicit surface normals for  $\mathcal{L}_{\text{normal}}$  defined in eq. (4) and positive samples for  $\mathcal{L}_{\text{pull}}$  defined in eq. (6), respectively. The push margin  $m$  in eq. (7) is set to 1.5 for the first 1k iterations, and is later increased to 2. In Neural Parser, the DBSCAN epsilon is fixed to 0.2. We optimize plane parameters of local planar primitives using Adam optimizer with an exponential decay schedule from an initial learning rate of  $1 \times 10^{-3}$  to  $1 \times 10^{-4}$ .

## A.3 MORE DETAILS ON EXPERIMENTS

### A.3.1 DATASETS

In our experiments, two publicly available datasets, ScanNetv2 (Dai et al., 2017) and ScanNet++ (Yeshwanth et al., 2023), are used to evaluate our method as they offer surface reconstructions and densely annotated instance-level semantics that can be further processed (Liu et al., 2019) to obtain the ground truth. Specifically, we sample 8 scenes from the official validation set of ScanNetv2 and 4 scenes from ScanNet++. All frames are resized to a resolution of  $640 \times 480$ . For each scene from ScanNetv2, one-eighth of the frames are uniformly selected for reconstruction, while in ScanNet++, equally spaced frames are downsampled according to the number of registered frames, leaving 150~279 frames per scene. Tab. 4 lists more details of the 12 selected scenes.

### A.3.2 IMPLEMENTATION DETAILS ON BASELINE METHODS

All the baseline methods are implemented following the official codebases and instructions. FineRecon (Stier et al., 2023) recovers accurate surfaces by introducing a depth guidance strategy, and here we use the multi-view depth predicted by SimpleRecon (Sayed et al., 2022) for such additional prior. Besides, as pointed by Yu et al. (2022b), the MLP architecture is inherently robust to motion blur and noisy camera poses due to its “smoothness bias”. Thus, we adopt the MLP variant of MonoSDF

Table 4: **Details of selected scenes.** For each scene, we downsample the video to a lower frame rate. *Down. Rate* denotes the downsample rate. *Area* is the surface area of ground-truth mesh.

	Scene ID	Type	# of Frames	Down. Rate	Area (m <sup>2</sup> )
ScanNetv2	0084.00	bathroom	247	12.5 %	42.68
	0164.03	kitchen	140	12.5 %	28.97
	0217.00	bedroom	156	12.5 %	40.65
	0316.00	lounge	97	12.5 %	26.56
	0356.00	bedroom	170	12.5 %	27.77
	0427.00	conference room	165	12.5 %	24.11
	0488.01	kitchen	137	12.5 %	38.53
	0568.00	lounge	207	12.5 %	71.49
ScanNet++	f6659a3107	conference room	181	1.8 %	133.38
	31a2c91c43	bathroom	184	2.4 %	31.72
	7bc286c1b6	bathroom	150	3.3 %	25.13
	303745abc7	office	279	4.4 %	63.43

for experiments on ScanNetv2, while in ScanNet++ with high-quality RGB captures, we use the Multi-Res.Grid variant for faster convergence.

The Sequential RANSAC employed in baselines and our method is all adopted from PlanarRecon (Xie et al., 2022), with thresholds specifically fine-tuned for each method. We render per-pixel depth map for each RGB keyframe using geometries given by various baseline surface reconstruction methods so as to combine these methods with AirPlanes (Watson et al., 2024).

### A.3.3 EVALUATION PROTOCOL

As several methods such as FineRecon (Yu & Lafarge, 2022) can predict geometry for unseen regions, we mask out these regions via a visibility check, and only preserve the observed areas for a fair evaluation. Tab. 5 (a) lists the metrics in geometry, where  $\mathbb{P}$  and  $\mathbb{P}^*$  are point clouds evenly sampled from the predicted and ground-truth mesh, each consisting of 200 000 points.

To assess how well the plane reconstruction aligns with the ground-truth semantics, we follow the evaluation protocol of PlanarRecon (Xie et al., 2022), reporting segmentation quality using three typical metrics. These metrics are listed in Tab. 5 (b) and were originally used for comparing partitions (Meila, 2005; Arbeláez et al., 2011). The ground-truth clustering  $\mathbb{C}^*$  is the partition of the ground-truth mesh into sets  $\mathcal{C}_1^*, \mathcal{C}_2^*, \dots, \mathcal{C}_{K^*}^*$ , where  $\mathcal{C}_i^*$  represents the collection of vertices of the  $i$ -th ground-truth planar primitive. The predicted clustering  $\mathbb{C}$  is obtained by partitioning *ground-truth vertices* according to the plane IDs of their nearest neighbors in the *predicted mesh*. The total number of vertices in the ground-truth mesh is denoted by  $N_{\mathbb{C}}$ .

- *Rand Index* represents the probability that  $\mathbb{C}$  and  $\mathbb{C}^*$  agree on the clustering of a randomly selected pair of vertices, where  $N_{\text{disagree}}$  is defined as the number of pairs that are clustered differently by  $\mathbb{C}$  and  $\mathbb{C}^*$ .
- *Variation of Information*, the sum of the entropies of  $\mathbb{C}$  and  $\mathbb{C}^*$  minus the mutual information between them, measures the distance between two partitions by information difference.
- *Segmentation Covering* is the average of mutual *coverings* between  $\mathbb{C}$  and  $\mathbb{C}^*$ , where the *covering*  $C(\mathbb{C}^* \rightarrow \mathbb{C})$  is computed as:

$$C(\mathbb{C}^* \rightarrow \mathbb{C}) = \frac{1}{N_{\mathbb{C}}} \sum_{\mathcal{C} \in \mathbb{C}} |\mathcal{C}| \cdot \max_{\mathcal{C}^* \in \mathbb{C}^*} \text{IoU}(\mathcal{C}, \mathcal{C}^*).$$

### A.4 MORE EXPERIMENTAL RESULTS

**Ablating Feature Dimension of NCF.** We investigate the performance of our proposed NeuralPlane when using different feature dimensions  $d$ . Specifically, we evaluate the effect of varying  $d$  from 1 to 128 using F-score, VOI, and SC metrics on ScanNetv2 dataset. As illustrated in Fig. 10, the

Table 5: **Definitions of metrics.** The quality of 3D plane reconstruction is evaluated by both geometry and segmentation metrics.

(a) Evaluation Metrics for Geometry.		(b) Evaluation Metrics for Segmentation.	
Metric	Definition	Metric	Definition
Accuracy	$\text{mean}_{p \in \mathbb{P}} (\min_{p^* \in \mathbb{P}^*} \ p - p^*\ _2)$	Rand Index	$\frac{N_C(N_C - 1) - 2N_{\text{disagree}}(C, C^*)}{N_C(N_C - 1)}$
Completeness	$\text{mean}_{p^* \in \mathbb{P}^*} (\min_{p \in \mathbb{P}} \ p - p^*\ _2)$	Variation of Information	$H(C) + H(C^*) - 2I(C, C^*)$
Chamfer	$(\text{Accuracy} + \text{Completeness}) / 2$	Segmentation Covering	$\frac{C(C^* \rightarrow C) + C(C \rightarrow C^*)}{2}$
Precision (%)	$\text{mean}_{p \in \mathbb{P}} (\min_{p^* \in \mathbb{P}^*} \ p - p^*\ _2 < 0.05) \times 100$		
Recall (%)	$\text{mean}_{p^* \in \mathbb{P}^*} (\min_{p \in \mathbb{P}} \ p - p^*\ _2 < 0.05) \times 100$		
F-score (%)	$2 \times \text{Precision} \times \text{Recall} / (\text{Precision} + \text{Recall})$		

performance of NeuralPlane is almost optimal when  $d$  is larger than 2. Similar results are also observed by ContrastiveLift (Bhalgat et al., 2023) and AirPlanes (Watson et al., 2024). In light of this, we simply choose  $d = 4$  in our experiments for a trade-off between performance and efficiency.

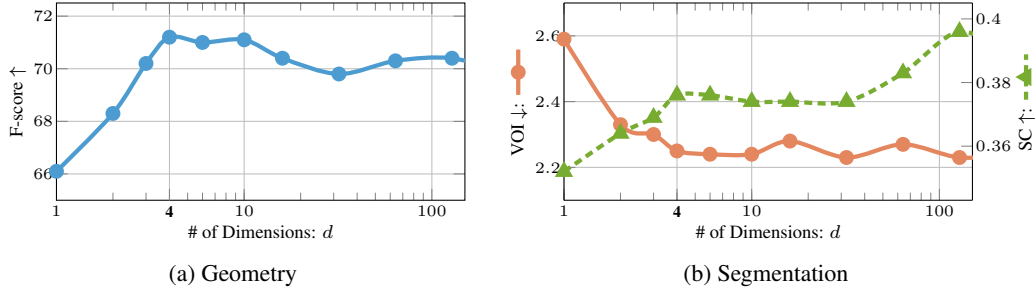


Figure 10: **Impact of different numbers of feature dimension.**

**Ablating DBSCAN Epsilon.** To supervise the neural parser module, our proposed method uses DBSCAN to first cluster the noisy primitive-level features rendered during each iteration. The study on the impact of varying the DBSCAN epsilon is presented in Fig. 11. The results indicate that the performance of NeuralPlane is close to optimal when the epsilon is in the range of 0.2 to 0.5. A higher cluster epsilon leads to coarse-grained feature discrimination, while a lower epsilon may result in over-segmentation. However, thanks to the robust mechanism of point grouping and parameter estimation introduced in Sec. 3.3, no significant performance deterioration is observed even if DBSCAN is ineffective (with the cluster epsilon set to 2).

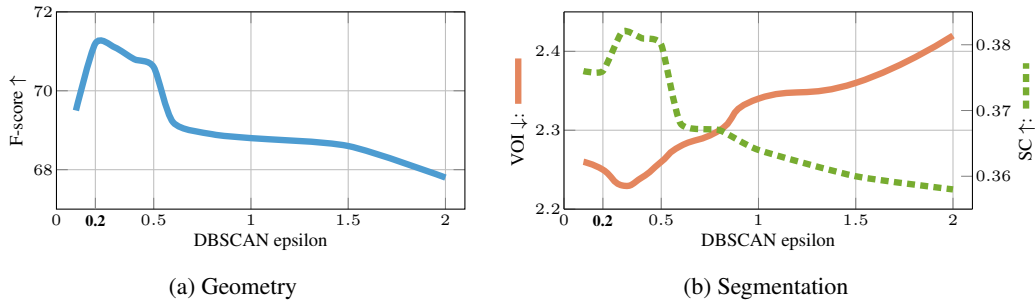


Figure 11: **Performance on ScanNetv2 with varying DBSCAN epsilon.**

**A Sensitivity Analysis of SfM Geometry.** Incorporating geometric cues, such as estimated monocular depth and normal maps, into neural scene representations is widely adopted to improve the performance of indoor 3D surface reconstruction (Yu et al., 2022b; Wang et al., 2022; Park et al., 2024). Likewise, NeuralPlane requires additional geometric priors for the initialization of local planar primitives. We find that, although sparse and noisy, the readily available SfM point cloud is sufficient to provide a good initialization. To further analyze the robustness of our approach to

SfM geometry of different quality levels, we utilize different SfM point clouds triangulated from correspondences estimated with various feature matching techniques. Results in Tab. 6 demonstrate that dense matching methods, *e.g.*, LoFTR (Sun et al., 2021), are more favorable for our method, as sparse matching methods, *e.g.*, SuperPoint (DeTone et al., 2018) + LightGlue (Lindenberger et al., 2023), are struggling with low-texture regions. Besides, our approach can consistently benefit from the development of more advanced feature matcher, *e.g.*, RoMa (Edstedt et al., 2024).

Table 6: Performance of NeuralPlane initialized with different SfM keypoints.

Method	Geometry		Segmentation		
	Chamfer ↓	F-score ↑	RI ↑	VOI ↓	SC ↑
w/o SfM Geometry	10.13	40.2	0.925	3.08	0.293
SuperPoint + LightGlue	5.90	65.4	0.942	2.49	0.345
LoFTR (Indoor)	<b>4.57</b>	72.8	<b>0.956</b>	2.24	0.380
LoFTR (MegaDepth) ← in main paper	4.59	71.2	0.955	2.25	0.376
RoMa (Indoor)	4.62	<b>73.2</b>	<b>0.956</b>	<b>2.12</b>	<b>0.400</b>

**Evaluation on Reconstruction Efficiency.** In contrast to learning-based MVS methods that can be implemented online at interactive speeds, our proposed NeuralPlane is a relatively time-consuming method that requires per-scene optimization. However, our method is much more efficient than other offline neural surface reconstruction methods. Tab. 7 presents a comparison of average execution time against baseline models on ScanNetv2.

Table 7: Comparison of time consumption across neural implicit methods.

	Pre-processing (min)	Training (h)	Inference (min)
ManhattanSDF (Guo et al., 2022)	44.5	5.6	2.3
NeuRIS (Wang et al., 2022)	0.5	4.2	1.2
MonoSDF (MLP) (Yu et al., 2022b)	<b>0.3</b>	7.5	0.7
NeuralPlane	2.9	<b>0.1</b>	<b>0.5</b>

**Additional Qualitative Results.** In Figs. 12 and 13, we visualize the entire 3D plane reconstruction on ScanNetv2 and ScanNet++ datasets, drawing comprehensive comparisons against state-of-the-art methods. Moreover, we provide close-up views rendered from reference poses in Fig. 14.

**Out-of-Domain Experiment.** While our work primarily focuses on indoor scenarios, we also conducted experiments on two small-scale outdoor scenes from the Niantic MapFree dataset (Arnold et al., 2022). The results in Fig. 15 highlight the potential of our method to generalize to outdoor environments.

## A.5 LIMITATIONS AND FUTURE WORK

**Failure Cases.** Fig. 16 illustrates several common failures, showcasing issues such as (a) missing structures and (b) under-segmentation, both of which stem from inaccuracies in 2D plane observations. The method is also not equipped to handle (c) non-planar surfaces. Besides, manually setting the number of semantic prototypes limits the adaptability of our method; for instance, an excessively large value may lead to (d) over-segmentation.

NeuralPlane at its core is integrating noisy 2D plane observations into a unified 3D neural representation, but it may fail to recover from catastrophic errors such as severe inaccuracy in mono-normal estimation and SfM geometry, which we did not consider. Meanwhile, the method is currently restricted to compact environments and better suited to indoor settings. Complex and large-scale scenes continue to pose many challenges, including (1) the need for large model capacities, and (2) the presence of massive non-planar clutter, which we leave for future research. Intersection analysis (Nan & Wonka, 2017) or integrating other cues such as occlusion edges for more structured reconstruction is another interesting research topic. It is also promising to implement our method in an online and efficient SLAM framework (Zhu et al., 2022; Matsuki et al., 2024).



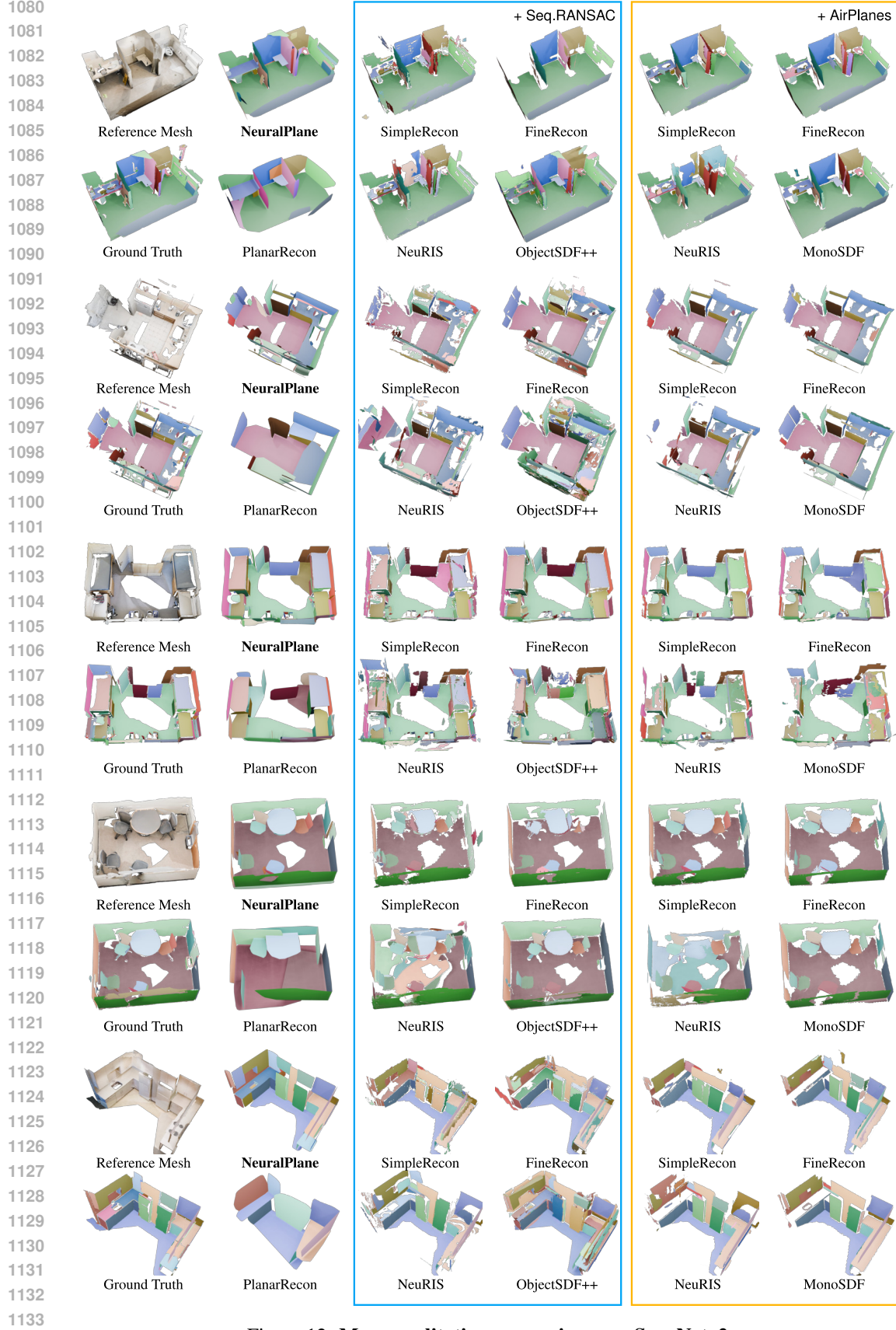


Figure 12: More qualitative comparisons on ScanNetv2.

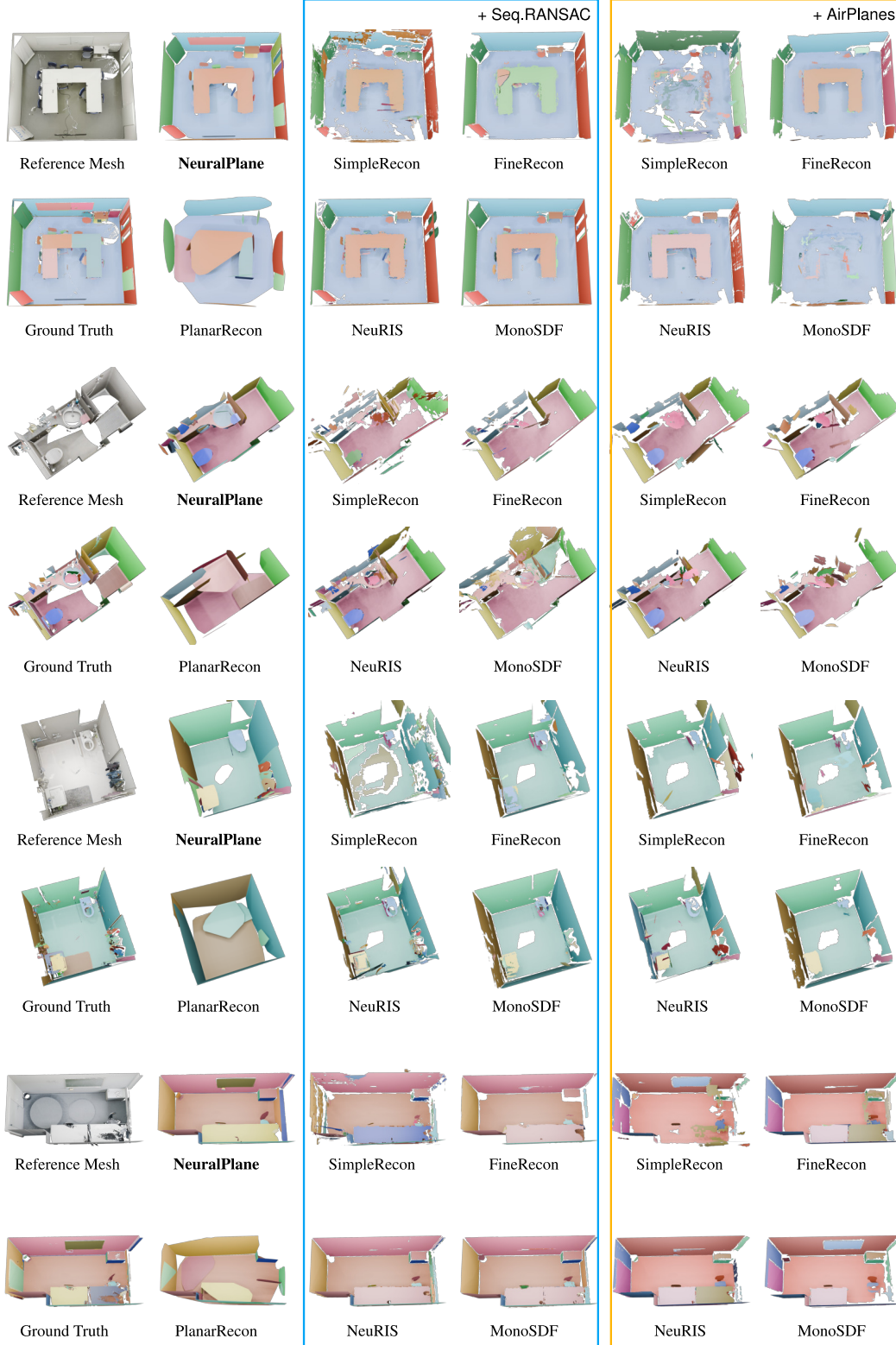


Figure 13: More qualitative comparisons on ScanNet++. Ceilings and occluding walls have been removed for better visualization.

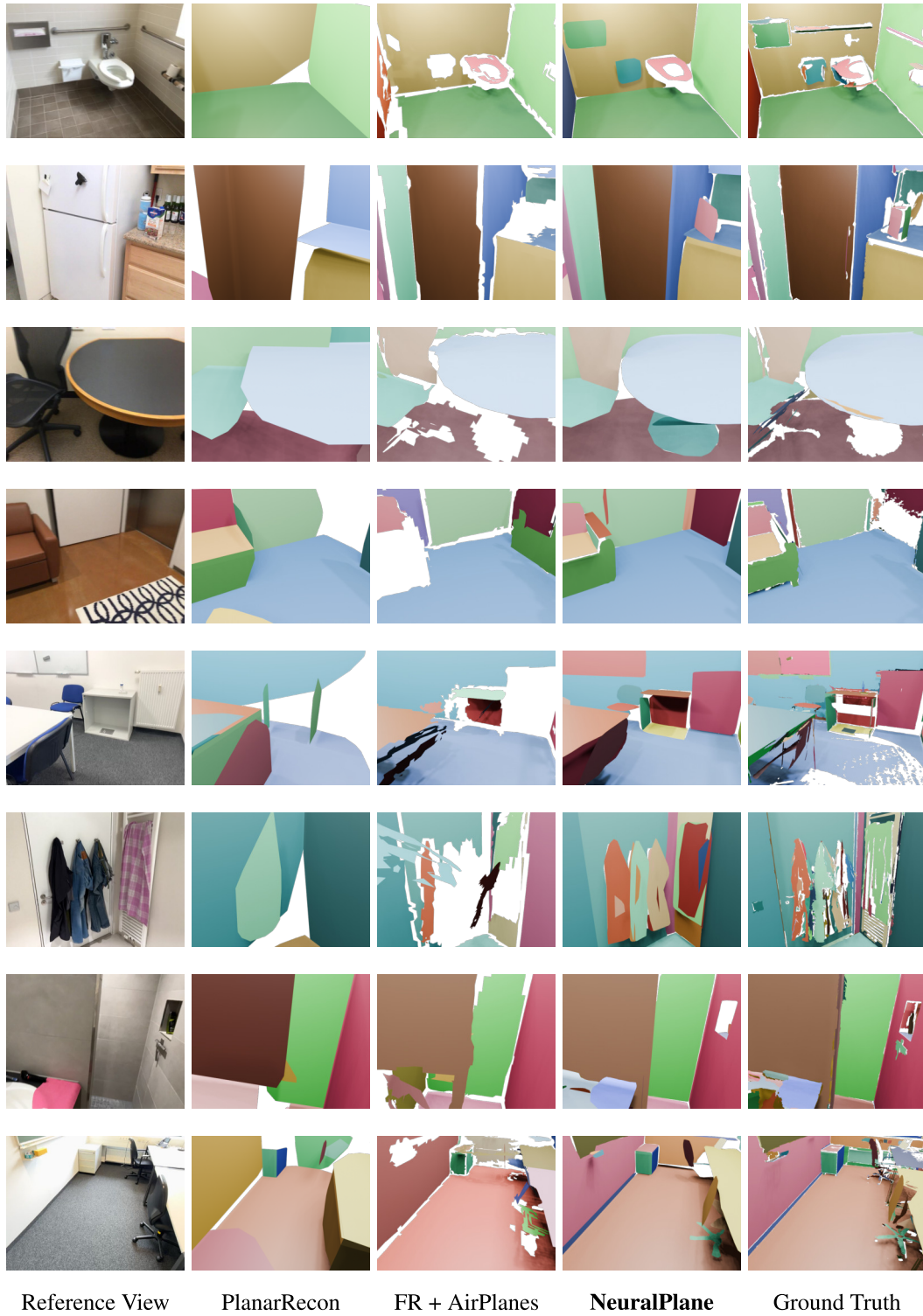


Figure 14: Close-ups of qualitative results.



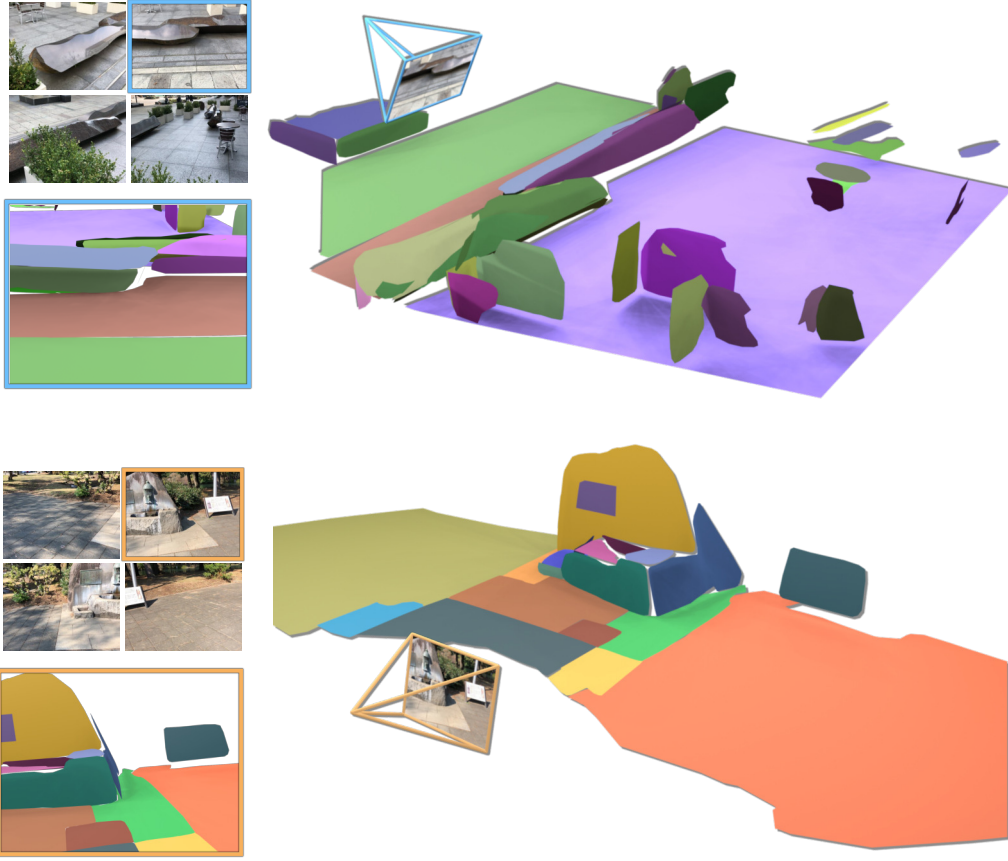


Figure 15: Our method generalizes to outdoor environments.

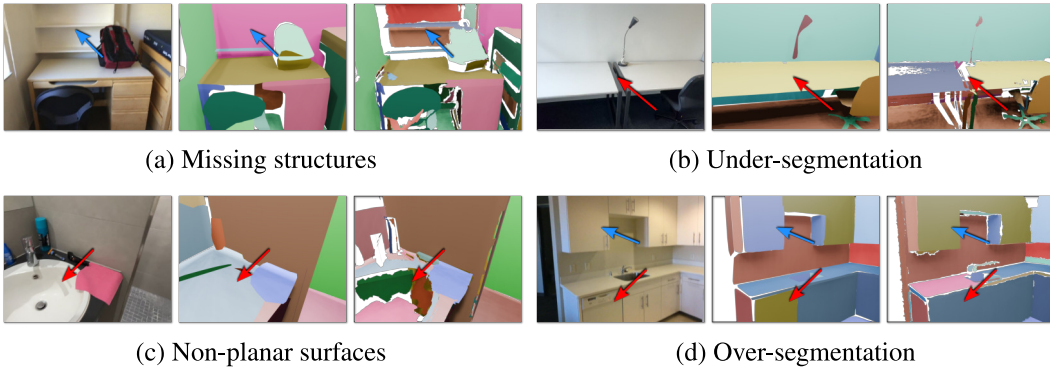


Figure 16: **Failure Cases.** In each case, from left to right: reference image, our reconstruction, and the ground truth. (a) Planes nearing the optical axis, as well as intricate structures, are difficult to detect in 2D and are thus likely to be absent from the final reconstruction. (b) The failure to semantically differentiate between two adjacent planes in certain views could lead to under-segmentation. (c) Non-planar surfaces are forcibly fitted into planes. (d) Over-segmentation due to a too large value of semantic prototypes.